CHALMERS
UNIVERSITY OF TECHNOLOGY

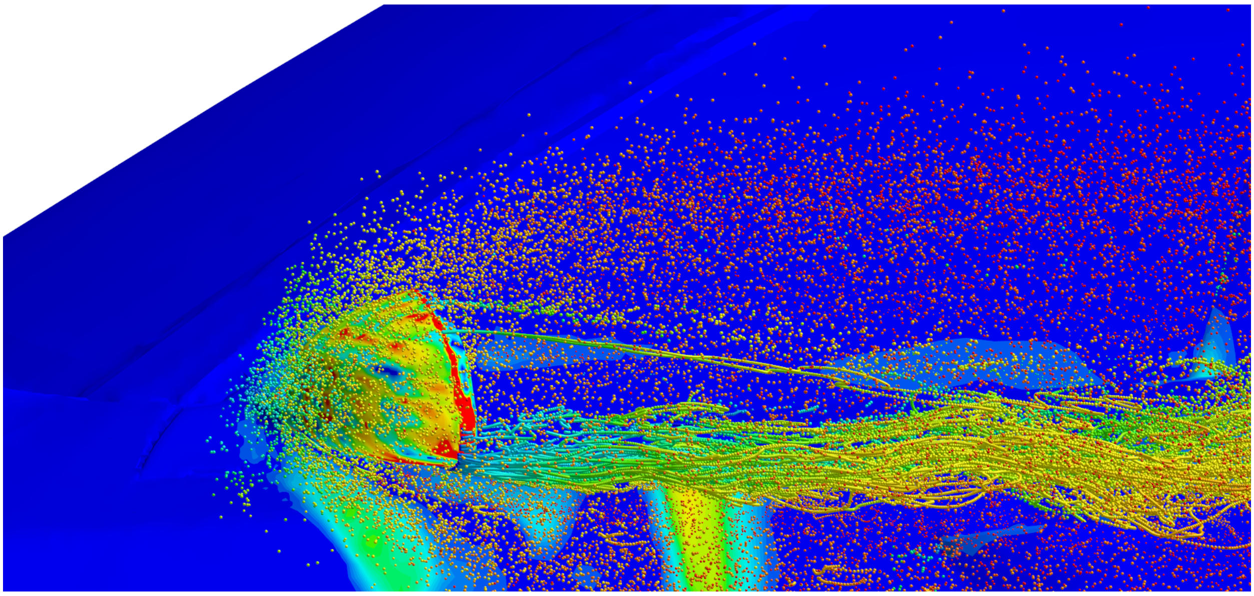

Eulerian-Lagrangian Modeling of contamination on exterior of a NEVS Vehicle

Master's thesis in Fluid Dynamics

HAMED HAMID ELAMIN
ISHAAN MARKALE

Department of Mechanics and Maritime Sciences
CHALMERS UNIVERSITY OF TECHNOLOGY
Gothenburg, Sweden 2017

Master's thesis 2017:70

Eulerian-Lagrangian Modeling of contamination on exterior of a NEVS Vehicle

HAMED HAMID ELAMIN
ISHAAN MARKALE

CHALMERS
UNIVERSITY OF TECHNOLOGY

Department of Applied Mechanics
Division of Fluid Dynamics
Chalmers University of Technology
Gothenburg, Sweden 2017

Eulerian-Lagrangian Modeling of contamination on exterior of a NEVS Vehicle

HAMED HAMID ELAMIN ISHAAN MARKALE

Supervisors: Dr. Mohammad El-Alti, NEVS AB and Johan Pilqvist, NEVS AB
Examiner: Professor Srdjan Sasic, Department of Applied Mechanics

Master's Thesis 2017:70
Department of Mechanics and Maritime Sciences
Division of Fluid Dynamics
Chalmers University of Technology
SE-412 96 Gothenburg
Telephone +46 31 772 1000

Cover: The flow of droplets around the rear-view mirror of a NEVS 9-3 model. The droplets are colored from blue to red by their velocity, from 0 m/s to 14 m/s and sized by their diameter, from 0 mm to 0.8 mm. The surface of the vehicle is colored from blue to red by the fluid film thickness, from 0 mm to 1 mm.

Chalmers Reproservice
Gothenburg, Sweden 2017

Eulerian-Lagrangian Modeling of contamination on exterior of a NEVS Vehicle
HAMED HAMID ELAMIN ISHAAN MARKALE
Department of Mechanics and Maritime Sciences
Division of Fluid Dynamics
Chalmers University of Technology

Abstract

The rear view mirror design plays an important role for the resulting cleanliness of the driver's side-window when cruising in rainy conditions. The visible field and the mirror glass must be as clean as possible. The flow around a rear-view mirror is inherently unsteady and vortex dominated. The contaminant particles (rain droplets) hit the mirror body and moves as wall film to a separation point that is governed by the mirror design. When the droplets separate, they can either enter the mirror wake or follow the ambient flow to leave the car. In this thesis, the complete process was modeled. It is shown how mirror design can be used to minimize the contamination areas to have maximum visibility. First, a benchmark study was done to understand the governing parameters of droplet and fluid film flow on a simplified geometry using the CFD software Star-CCM+. The flow was modeled using unsteady RANS and droplets were tracked using Lagrangian Particle Tracking (LPT). The conclusions from the benchmark study were implemented on the full vehicle model of NEVS vehicle. The simulation results were compared with a contamination test performed at NEVS climate tunnel.

Keywords: NEVS, Film Modeling, Film separation, Lagrangian Particle Tracking, Contamination, Rear view mirror design.

Preface

This report describes the master thesis work done by Hamed Hamid Elamin and Ishaan Markale as a part of the master thesis in Applied Mechanics at Chalmers University of Technology, Gothenburg. The work was performed at NEVS AB in Trollhättan under the supervision of Dr. Mohammad El-Alti and Johan Pilqvist. The thesis opposition was done by Ömer Faruk Cavusoglu and examined by Prof. Srdjan Sasic from the Division of Fluid Dyanmics, Chalmers University of Technology.

Acknowledgements

We would like to thank Dr. Mohammad El-Alti for giving us the opportunity to work on a interesting and challenging multiphase flow problem and guiding us throughout the thesis. A special thanks to Johan Pilqvist for the fruitful discussions and providing valuable feedback and pointing us in the correct direction whenever we faced any problems. We would also like to express our gratitude towards Prof. Srdjan Sasic for sparkling the interest in multiphase flow problems, teaching us the modeling techniques and an objective view of the challenges and problems involved. Thanks to CD-Adapco and especially Leonardo Palma for providing all the Power-on-demand license hours and modeling related issues in Star-CCM+. To all the colleagues at NEVS, thank you for all the fascinating discussions over lunch and coffee breaks. Finally, many thanks to all friends and family for supporting us throughout.

Hamed Hamid Elamin & Ishaan Markale
Gothenburg
June 2017

Contents

List of Figures

List of Tables

1

General Introduction

This master's thesis was carried out at National Electric Vehicle Sweden (NEVS) in Trollhättan. NEVS was formed in 2012 after acquiring Saab Automobile AB. The company focuses on developing electric vehicles exclusively. NEVS does not only wants to develop the next generation of electric vehicles, but also smart mobility solutions for a sustainable future.

Today's electric vehicles are limited by their battery capacity. Therefore, aerodynamics plays a crucial role in developing a new electric vehicle since the drag contributes a major chunk of energy consumption from the battery. The rear view mirror plays a crucial role in determining the coefficient of drag C_D of the car. The design of the rear view mirror also plays a crucial role in maintaining the visibility of the driver's side window when the vehicle is traveling in rainy conditions. This thesis focuses on how the mirror design affects visibility.

1.1 Background

Whenever a new vehicle is to be developed, the management of rain water on the external surface of the vehicle needs to be taken into consideration in the designing process. The studies conducted for analyzing this are called external rainwater management (EWM) or vehicle soiling studies. The A-pillar and the rear view mirror design plays a key role in determining the flow of water on the exterior of the vehicle, especially the driver's side window [1]. When a vehicle is driven in rainy conditions, the driver's side window and the rear view mirror glass are affected by contamination due to rain droplets [2] (see Figure[1.1]). Consequently, the driver's side window and the mirror glass must be as clean as possible in order to increase active safety. Maintaining the visibility on the side windows and the mirror glass leads to improved driver safety and comfort.

Experimental investigations of EWM are difficult for vehicle manufacturers since it requires a detailed full scale vehicle model and a wind tunnel for testing. Each time problems are identified in a design, new prototypes need to be manufactured in order to test them. Another experimental method available is on-road testing. However, there are many drawbacks to this. The major issue is the non repeatability of the driving conditions, no quantitative information of flow characteristics and most importantly, the skepticism of car manufacturers to reveal new car models. Consequently, car manufacturers want to minimize the cost of testing and validation of mirror and A-pillar designs. Performing a numerical simulation allows the car manufacturer to analyze the fluid flow problems in detail, which is not possible in a wind tunnel test. Hence, it is easier to take design decisions earlier in the design cycle. Numerical methods for investigation EWM

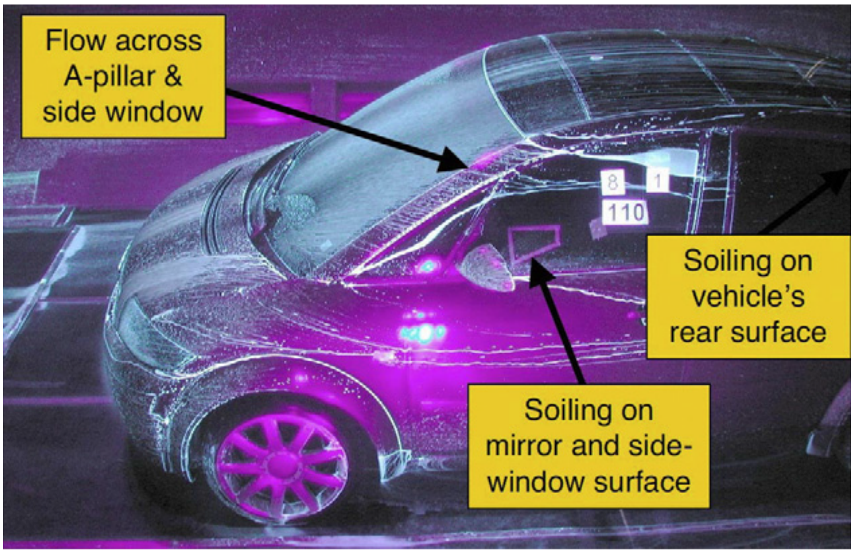

Figure 1.1: Wind tunnel test of contamination [2]

are therefore preferred as they lead to a reduction in development costs.

1.2 Objectives

The aim of this thesis was to first understand the governing flow phenomena occurring around the the rear view mirror when cruising in rain. The next step was to identify methods for modeling these phenomena using the CFD solver Star-CCM+ and predict how the design of the mirror can be used to minimize the contamination areas to achieve higher visibility for the driver. Consequently, the objective of the thesis work is to strengthen the knowledge of multiphase flows at NEVS and develop a methodology for performing contamination simulations. The results from this methodology are finally compared to a contamination test on the NEVS 9-3 model.

In order to understand the flow of rain droplets over side view mirror and driver side windows, the numerical studies of EWM must consider the following phenomena (see Figure [1.2]):

- The flow of air and rain droplets aound the vehicle
- Coupling between the air and water droplets
- Wall impingement and near wall interaction of droplets
- Fluid film formation, its instability and breakup
- Droplet trajectories in separation region

Suitable modeling approaches to model the governing phenomena need to be found. The selected approach should be computationally feasible while at the same time give an accurate enough result which can be validated by experiments.

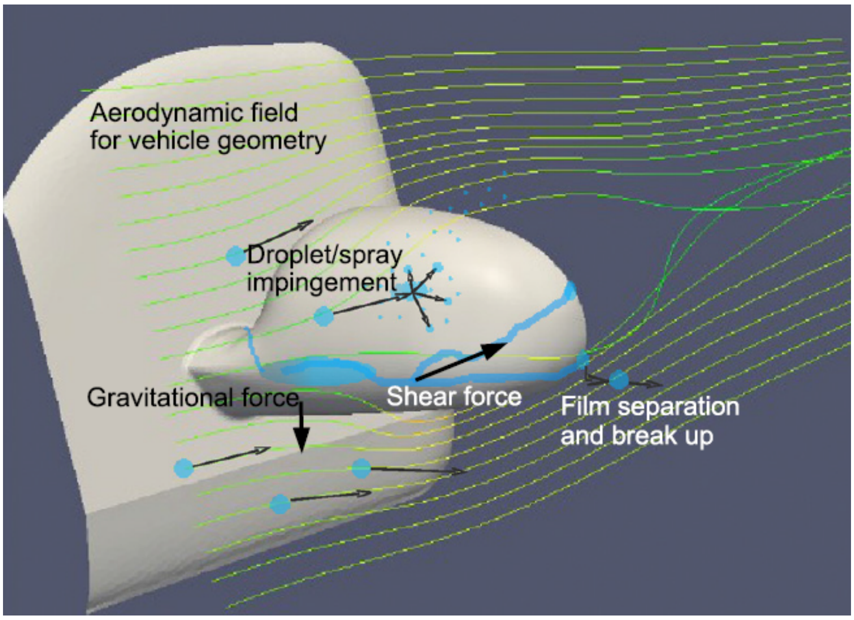

Figure 1.2: Governing physical phenomena in EWM [2]

1.3 Limitations

The objective is to investigate key parameters which govern the flow of rain droplets around the mirror and identify modeling techniques rather than optimization of the mirror design. The chosen numerical technique is the Eulerian-Lagrangian method. Theoretically, this method is valid only for very low volume fractions of the Lagrangian phase, but it still has been used for higher volume fraction assuming the point source approximation [5]. The CFD solver Star-CCM+ is utilized for performing the simulations, hence only the modeling parameters available in this software are investigated. A balance was sought between having accurate enough solution and reducing computational time required. Further, the experiments performed are compared only qualitatively with the simulation results.

1.4 A guide through the chapters

In Chapter 2, a description of the modelling techniques used to simulate water droplets and film formation is provided. Chapter 3 provides the details of the numerical modeling techniques applied on a simple test case geometry and the numerical parameters studied. Chapter 4 looks at the simulation methods applied on the full vehicle model and comparisons are made between the simulations and full scale wind tunnel test results. Chapter 5 finally summarizes the work done and further possibilities of work to be done.

2

Numerical Modeling of droplets and fluid film

This chapter provides the reader a background about modeling multiphase flow of droplets in air and about fluid film modeling.

A phase refers to the solid, liquid or vapor state of matter. The flow of air around a car is an example of a single-phase flow. Single phase flow has been a research topics for many years. The equations for the motion of single-phase fluids are well accepted (the Navier-Stokes equations) and closed solutions for some cases are established. The main challenge is to model the turbulence and its affect on mass, momentum and energy transfer [5]. Multiphase flows refer to flow problems where there is a simultaneous presence of different phases (gas, liquid or solid) in the domain of interest. Compared to single phase flows, the level of development for multiphase flows is considerably less i.e. the formulation of the some of the governing equations is still up to debate. It also involves complicated and collective behaviour of a large number of interacting degrees of freedom. Hence, analyzing multiphase flows is a challenging prospect.

Table 2.1: Categories of multiphase flows

Gas-Liquid Flows	Bubbly flows
	Separated flows
	Gas-droplet flows
Gas-Solid Flows	Gas-particle flows
	Fluidized beds
	Pneumatic transport
Liquid-Solid Flows	Slurry flows
	Hydro-transport
	Sediment transport
Three phase Flows	Droplets/Particles in gaseous flows

Multiphase flows can be subdivided into four categories: gas-liquid, gas-solid, liquid-solid and three-phase flows (see Table[2.1]). A flow is said to be a dispersed phase flow when one phase is dispersed and the other is continuous. A path can be traversed in the continuous phase from one point to another without crossing into the other phase. Consider the flow of droplets in air. It is not possible to pass from one droplet to another without going through the air. Gas-droplet flows are hence categorized as dispersed flows. A separated flow is one in which the phases are continuous for example, a liquid moving along the bottom of a pipe and the gas along the top.

2.1 Eulerian-Lagrangian modeling of multiphase flow

The subject of this thesis is to study the flow of rain droplets around a vehicle geometry. The focus will be laid on the the impingement of droplets on the rear-view mirror, the formation of fluid film on the mirror housing and its subsequent development and separation into droplets from the edges of the mirror housing. The CFD software package Star-CCM+ will be utilized to simulate this phenomena.

The Eulerian-Lagrangian approach is used to denote a family of modeling and simulation techniques in which droplets or particles are represented in a Lagrangian reference frame while the carrier–phase flow field is represented in an Eulerian frame. In the framework for multiphase flows, the continuous phase (air) is solved for using the Navier-Stokes equations (Eulerian framework). For the discrete phase (droplets), Newton's equations of motion are solved by modeling the forces acting on each droplet. The effect of one phase on the other, also known as coupling, is applied by adding source terms in the governing equations for momentum, mass and energy for the fluid.

Difficulties are encountered by the EE (Eulerian-Eulerian) two–fluid approach to particle or droplet jets impinging on surfaces, and particle– or droplet–laden flows in regimes not dominated by collisions. This is because EE two–fluid formulations are not capable of representing the fluxes, and resulting physical phenomena, associated with two streams of particles (or droplets) moving with different velocities at the same physical location, whereas this is naturally incorporated in the EL approach. Also from a numerical standpoint, the EL approach minimizes numerical diffusion in dispersed–phase fields such as volume fraction and mean velocity when compared to grid–based Eulerian approaches [7].

2.1.1 Some relevant parameters

The particle Reynolds number Re_p is defined as $Re_p = \rho_c|v_c - v_p|d_p/\mu_c$, where ρ_c is the density of the continuous phase (air), v_p is the velocity of the particle (droplets), v_c is the velocity of air and μ_c is the dynamic viscosity of air [1]. The particle response time τ_p is defined as $\tau_p = \rho_p d_p^2/18\mu_c$ when $Re_p < 1$ (also called Stokes flow regime). Correction factors are introduced for higher Re_p [5]. The Stokes number St is defined as $St = \tau_p/\tau_c$, where τ_c is a characteristic time scale of the fluid flow. For $St << 1$ the particles have enough time to respond to changes in flow velocity. Thus the particle and fluid velocities will be in equilibrium. For $St >> 1$, the particles do not respond to changes in the flow velocity. St determines the strength of coupling between the phases. A general guideline for considering a flow dilute is $St < 1$ and dense for $St > 1$. [5]

2.1.2 Droplet-Fluid interaction

In the Lagrangian framework, the properties associated with the i^{th} particle (position, velocity, acceleration) are solved for. The forces are modeled and the equation of motion is solved individually for each droplet or parcel (see Section 2.1.4) to step-wise update its position. For an incompressible unbounded flow with translational velocity of particles (assumed to be small spheres) and a slow variation of characteristics ($Re_p << 1$), the equation of motion is given as [6]:

---

[1] subscript c denotes continuous phase and p denotes particulate phase

$$m_p \frac{d\boldsymbol{u_p}}{dt} = \sum \boldsymbol{F_i} \tag{2.1}$$

The forces acting on the particles are given by:

- **Pressure Gradient Force**: The local pressure gradient in the flow creates a force in the direction of the pressure gradient. The total pressure force acting on a particle can be integrated over its surface and can be written as as $F_{p,i} = \int_{cs} -pn_i dS$. Applying the divergence theorem and assuming the pressure gradient is constant over the volume of the particle gives:

$$F_{p,i} = -V_p \frac{\partial p}{\partial x_i} \tag{2.2}$$

- **Buoyancy Force**: This is force acting on the particles due to the amount of fluid they have displaced. It is given by:

$$F_b = \rho_c g V_p \tag{2.3}$$

  This force does not contribute significantly to the motion of a particle in gas-droplet flows where the ratio of material densities is generally of the order of 10^{-3}. [5]

- **Drag Force**: The steady state drag force is calculated assuming that there is no acceleration of the relative velocity between the droplet and the air. The effects of curvature of the velocity of the air are also neglected. The expression is given by:

$$F_D = \frac{1}{2}\rho_c C_D A|v_c - v_p|(v_c - v_p) \tag{2.4}$$

  where C_D is the drag coefficient and A is the reference area of the droplet (projected area in the direction of droplet velocity). The drag coefficient is a function of Re_p, droplet shape, closeness to walls and other droplets etc. Figure[2.1] shows the variation of C_D with Re_p. [9]

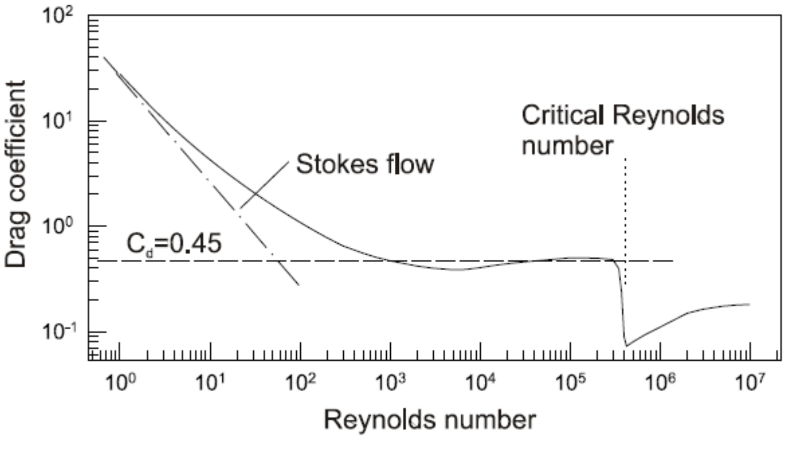

Figure 2.1: Variation of the C_D of a sphere with Re_p [9]

Several correlations are available for C_D as a function of Re_p. The Schiller-Naumann correlation [10] (Equation 2.5) is often used for spherical water droplets and small bubbles (for $Re_p < 1000$). It gives less than 5% variation [5] from the standard drag curve shown in Figure[2.1].

$$C_D = \left(\frac{24}{Re_p} (1 + 0.15 Re_p^{0.687}) \right) \tag{2.5}$$

Droplet distortion due to aerodynamic effects increases the drag due to the sphere turning into a more disk-shaped object. The Liu dynamic drag coefficient [11] is used to model the distortion effects. Intermediate shapes between a disk and a sphere are interpolated using the radial displacement normalized by the droplet diameter [14] to give the expression, $C_D = C_{D_{sphere}}(1 + 2.632y)$, where y is the interpolation factor, which is 0 for a sphere and 1 for a disk.

- **Virtual Mass Force**: When an object is accelerating/decelerating inside a fluid, there is an opposite effect on the surrounding fluid because the moving object needs to displace a certain volume of the fluid. Therefore, more force is required to move the object in a fluid compared to in vacuum. This gives an additional inertia to the object which is called the added mass. The fluid is gaining energy at the expense of work done by accelerating the object

$$F_{vm} = m_p \frac{\rho_c}{\rho_p} \frac{d}{dt} (v_c - v_p) \tag{2.6}$$

- **History Force**: This force involves the viscous effects due to a boundary layer development when the relative velocity between the phases is changing. Due to this changing velocity and unsteadiness, there is a delay in this boundary layer development on the surface of the particle. Hence, the boundary layer never gets fully developed around the particle. This is the physical source of the history force. It is called the history force as it depends on how the particle has behaved up to a particular time instant.

- **Lift Forces**: Lift forces are due to the pressure distribution developed on a particle in a velocity gradient. A higher velocity on one side of the particle gives rise to a low pressure, and the high pressure on the low velocity side gives rise to a lift force. This is called as the Saffman lift force. Particle lift forces are also due to the rotation of particles. This is known as the Magnus force [5].

$$F_{Saff} = 1.61 \mu_c D |u_i - v_i| \sqrt{Re_G} \tag{2.7}$$

$$F_{Mag,i} = \frac{\pi}{8} D^3 \rho_c [\epsilon_{ijk} \omega_{d,j} (v_k - u_k)] \tag{2.8}$$

where

$$Re_G = \frac{D^2}{\nu_c} \frac{du}{dy} \tag{2.9}$$

2.1.3 Coupling between the phases

Coupling between the phases describes the property exchange between the continuous (Eulerian) phase and the dispersed (Lagrangian) phase. Coupling can take place through transfer of mass, momentum and energy between the phases. When the continuous phase affects the dispersed phase, while the dispersed phase does not affect the continuous phase in any way, the flow is considered to be one-way coupled. While for two-way coupling, the continuous and dispersed phases affect each other. In dense flows where the particles interact with each other, as well as the interaction between the dispersed and continuous phases, the flow is four-way coupled [5].

To determine if the flow should be one, two or four-way coupled some parameters need to be investigated. One method is to check the volume fraction of the dispersed phase. If it is less than 10^{-6}, one-way coupling is usually sufficient [5]. While for a flow with higher volume fraction than 10^{-6} but less than 10^{-3}, two-way coupling is suitable. These flows are considered dilute. An even higher volume fraction should be modelled with four-way coupling [2]. Another method for determining the strength of coupling is by calculating the momentum coupling parameter Π_{mom}. It represents the importance of momentum coupling, and can be estimated by:

$$\Pi_{mom} = \frac{C}{1 + St_{mom}} \tag{2.10}$$

where C is the ratio between the bulk density of the dispersed and continuous phase, and St_{mom} is the Stokes number for momentum transfer. As the Stokes number gets larger or the concentration becomes smaller, the momentum coupling becomes less important [5].

2.1.4 Statistical description of the Lagrangian phase

In the Eulerian-Lagrangian approach, the equation of motion of each particle is solved in order to track it. This is feasible when the number of particles are small. However, when the number of particles that need to be tracked are high, then it is computationally cheaper to use the parcel approach. A parcel can be thought of as a discretization of the Lagrangian phase. The dynamic properties for each particle in the parcel are the same i.e. diameter, velocity, temperature etc. The density of the parcel is assumed to be the same as that of the droplets. This means that there are no voids in any parcel. A parcel is also called a *computational particle*. The properties of the parcels are solved as they move through the field.

The number of parcels are lesser compared to the number of physical particles in the flow. The reduction in computational cost is achieved by assigning a statistical weight to the computational particles. The statistical weight is the average number of droplets represented by a parcel. This statistical weight or, the number of particles per parcel (N_P) must be determined before the simulations are run. N_P must be small enough so that the full characteristics of the droplets are captured. Simultaneously, this must be balanced with reducing the total number of parcels to keep the computational cost low. N_P depends on the size and the mass flow rate of the droplets [4]. Using the parcel approach allows for the modelling of turbulence dispersion, particle collision and agglomeration [5].

The flow field is discretized into a computational grid. Methods such as DNS and LES [7] can be used to solve the equations for the flow field. However, in this work, the Reynolds Averaged Navier-Stokes (RANS) equations have been solved for the flow field. The motion of each parcel over a time step is calculated integrating its equation of motion (Equation2.1). The time step has to be small enough so that any parcel only travels a small fraction of the size of any computational cell [5].

2.1.5 Turbulent Dispersion

Dispersion in a turbulent flow occur due to fluctuating fluid forces. The dispersion is caused by random forces that are continuous and vary in magnitude along the field. There are no dispersion caused by the mean fields. Effects of turbulence on the motion of the particle are important for small particles. In cases where the particles are small enough to follow the instantaneous fluid motion the particle dispersion is equal to the dispersion of the fluid element. Larger particles are unresponsive to turbulent velocity fluctuation [5].

Star-CCM+ uses the stochastic model by Gosman and Ioannides [20], which is similar to the random walk model. The turbulence is assumed to be isotropic and having a Gaussian probability distribution in the fluctuating velocity with a standard deviation of $\sigma_{ii} = (2k/3)^{1/2}$. The interaction time of the droplet and the randomly sampled velocity field needs to be determined. There are two possible events, either the droplet remains in the eddy during its whole lifetime

$$t_e = \frac{l_e}{|\mathbf{u'}|} \tag{2.11}$$

or it passes through the eddy in a transit time

$$t_R = -\tau ln\left[1.0 - \frac{l_e}{\tau|\mathbf{u} - \mathbf{u}_d|}\right] \tag{2.12}$$

Where τ is a relaxation time, l_e is the dissipation length scale, ϵ is the dissipation rate and C_μ is an empirical constant. The interaction time is chosen as the smallest of these two timescales, $t_I = min(t_R, t_e)$. When modeling turbulent dispersion by stochastic tracking a large number of simulations are needed. Hence an ensemble averaging is needed in order to gain a statistically significant sampling of the data.

2.1.6 Time step size

The parcel time step controls the accuracy of the Lagrangian multiphase solution. The purpose of the parcel time step is to advance the particle through the flow during a fluid time step and is calculated dynamically during each fluid time step. Calculation of the parcel time step is done using:

$$\frac{Co_{min}\Delta x}{max(|\mathbf{v}|, |\mathbf{v}_p|)} \leq \delta t_p \leq \frac{Co_{max}\Delta x}{max(|\mathbf{v}|, |\mathbf{v}_p|)} \tag{2.13}$$

Where Co is the Courant number, Δx is the characteristic length scale of a cell containing the parcel and $max(|\mathbf{v}|, |\mathbf{v}_p|)$ is the maximum velocity of either the fluid or the particle.

The parcel time step must be smaller than the fluid time step to get an accurate parcel tracking. The parcel should as well not traveling more than one cell size during each time step. Depending on the forces interacting on the particles, different model time scales propose restrictions on the parcel time step. Among these are the momentum relaxation time-scale from the drag force model and the residual of the eddy interaction time-scale from the turbulent dispersion model [4].

2.1.7 Secondary breakup of droplets

Droplet break-up is caused by aerodynamic forces (pressure and friction) induced by the relative velocity between the surrounding air and the droplets. An unstable growing of waves on the interface between the air/water or on the whole droplet is due to the aerodynamic forces. This unstable growth of waves leads to disintegration and creation of small droplets. These small droplets are yet again subjected to more aerodynamically induced break-up. This is countered by the surface tension force that tries to counter the deformation by keeping the droplets spherical. The surface tension force is dependent on the surface curvature, where a smaller droplet results in a larger surface tension force and a larger critical relative velocity. Thus, leading to disintegration and an unstable droplet deformation. A representation of this behavior is expressed by the Weber number,

$$We = \frac{(\rho_c u_{rel}^2 d)}{\sigma} \tag{2.14}$$

where ρ_c is the density of air, d is the droplet diameter prior to break-up, σ is the surface tension between gas and the droplet and u_{rel} is the relative velocity between the phases. Depending on the Weber number there are different droplet break-up modes. Critical Weber number for secondary break-up is $We \approx 12$, this is the limit for vibrational break-up. A further increase in Weber results in bag, bag/streamer, stripping and catastrophic breakup (see Figure[2.2]) [19].

2.1.8 Particle-Wall interaction

The Bai-Gosman model [15] is a spray impingement model for droplet/wall interaction in a Lagrangian framework. The characteristics of the impinging droplets and the outcome after impingement is the main focus of the model. The choice of the impingement regime is dependent on four parameters:

- The incident Weber number
- The Laplace number: $La = \sigma \rho L/\mu^2$
- The temperature of the boundary (wall)
- The state of the wall, i.e. dry or wet

For a wall with a temperature less than the boiling temperature of the fluid these following impingement regimes occur:

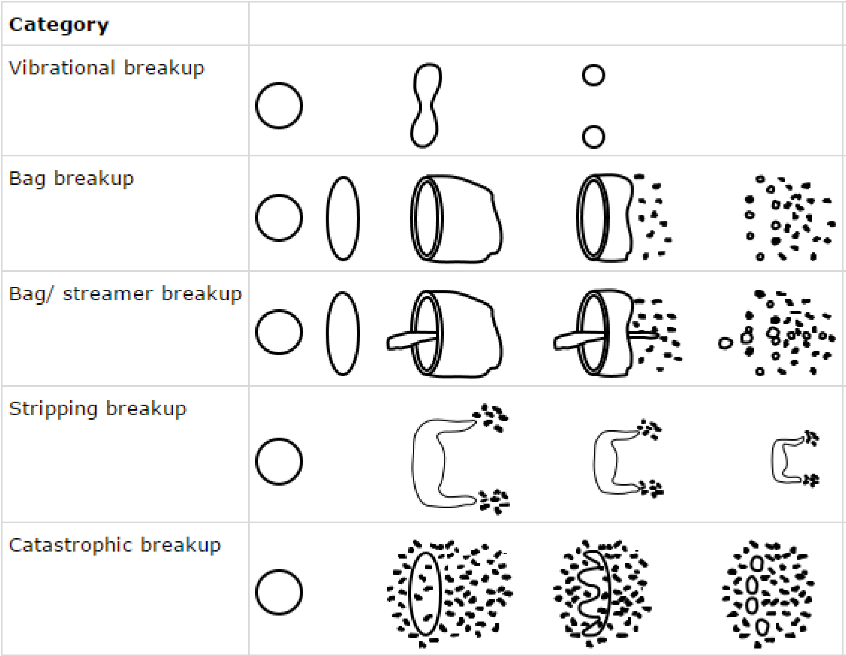

Figure 2.2: Secondary breakup of droplets [4]

- **Stick**: Impinging droplets stick to the wall in an almost spherical form. This regime occurs when the impact energy is very low and the Weber number is low.
- **Rebound**: The impinging droplets bounce off the wall after contact.
- **Spread**: Impinging droplets with a moderate velocity impinge on a wall and form a wall film if the wall is dry. Otherwise, the droplets merge with an existing liquid film.
- **Splash**: Impinging droplets with a very high impact energy hit the wall and rebound as smaller droplets. The number of child parcels for this regime can be controlled and the diameter of the parcels is selected from a Rosim-Rammler distribution [4].

The transition between the different regions in a specific temperature range is dependent on We. Depending on if the wall is wet or dry the transition regimes as well as the critical Weber number for transition differ. In Table[2.2] the transitions between the impingement regimes for a wall temperature less than the droplets boiling temperature is described. Where A is a surface roughness coefficient [4].

Wall regime	**Wet Wall**	**Dry Wall**
Stick	$We < 2$	-
Rebound	$2 < We < 20$	-
Spread	$20 < We < 1320La^{-0.18}$	$We < ALa^{-0.18}$
Splash	$1320La^{-0.18} < We$	$We > ALa^{-0.18}$

Table 2.2: Transition criteria

2.1.8.1 Particle-Film transition

The particle film transition model determines whether impinging droplets form a film on the wall or not. Depending on the nature of the problem a suitable transition criteria should be selected. Two criterions are available in Star-CCM+, coverage ratio and equivalent film thickness. Coverage ratio is the fraction of the cell wall covered by the droplets impinging on the cell. The impinging droplets are assumed to take a cylindrical form during impact with a spreading diameter $D_s = 0.613dWe^{0.39}$. The area covered is then calculated and divided by the area of the cell on the wall. If the ratio is larger than the coverage ratio, then all the droplets merge into a fluid film. For the purpose of this thesis, a more generally applicable criterion called the equivalent film thickness criterion is applied instead. The equivalent film thickness δe is a ratio between the total volume of all the droplets on a cell wall and the area of a cell, $\delta e = V_d/A_c$. When δe reaches the value given for the equivalent film thickness property, all the droplets merge into a liquid film [4].

2.1.9 Fluid Film Modeling

Fluid film formation as a result of spray impingement is a transition that normally occur during rainy conditions. Droplets impinge on a surface and slowly starts to form a film or merge with an existing film. The surface area increases continuously as the film spreads. Spreading happens due to the shear force in the film surface, tangential momentum and impact pressure due to the impinging droplets, and the body force because of wall acceleration (if present).

The governing equations for the wall film flow, mass, momentum and energy, are established in the boundary-layer framework. An interface conditions at the film-gas interface are derived from principles of continuity and thermodynamic equilibrium. At the liquid-wall contact area the continuity of temperature, no-slip condition and momentum equations are set as wall boundary conditions [24].

In Star-CCM+, the fluid film is modelled using a shell region where the fluid film flows. The shell region is a two dimensional surface domain that is one cell thick. Depending on the situation, the interaction between the fluid film and the surrounding environment can be complex. Further mathematical modeling is required to get the details of the developed flows for these interactions. Two of these interactions are edge and wave stripping [4].

Since the shell region is one cell thick, it is assumed that the film is thin enough so that the laminar boundary layer approximation applies. A parabolic velocity profile across the film is assumed. If the calculated fluid film thickness exceeds the first cell height next to fluid film boundary, then a transition to computationally expensive VOF methods is needed.

2.1.9.1 Edge stripping

When the fluid film is driven by the gas phase to the end of a surface with a sharp edge, breakup often occurs. The film separates from the surface and droplets are formed as the film leaves the edge. These droplets then continue to flow in the air. As the film approaches the corner, the momentum of the film strives to separate the film from the corner that is balanced by two surface tension force as well as a gravitational force. By considering conservation of linear momentum for steady conditions in the p-direction (see Figure[2.3]) the balance is satisfied.

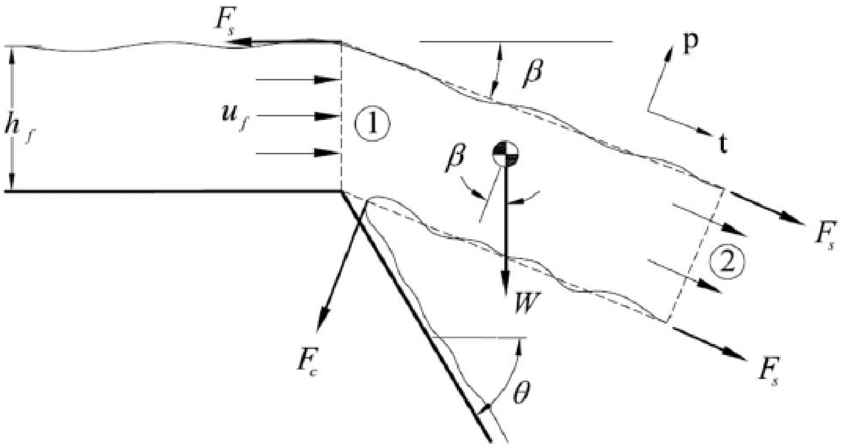

Figure 2.3: Edge stripping control volume

The separation of fluid film depends on various criteria:

- Free stream velocity
- Fluid film thickness h_f
- Minimum wall angle θ
- Film Reynolds number $Re_f = h_f u_f / \nu_f$
- Force Ratio - Ratio of inertial force to the surface tension force and the gravity force

The break-up of the fluid film into droplets is due to the aerodynamic force of surrounding air. The fluid film can ether separate or remain attached to the wall depending on if the break-up criteria is fulfilled for the inertia, surface tension and body forces. A force ratio of inertial force to the surface tension and the gravitational forces, normalized by the surface tension is used to determine if the film stays attached or stripping occurs. A force ratio of 1 is the criteria for the film separation, based on experiments performed by Friedrich et al [18]. If the ratio is above 1 the inertial force is large enough for the film to separate. Whereas if the ratio is less than one the film mass will remain attached to the wall [18]. In Star-CCM+ the droplets are separated from the edges using an injector. The film is ejected as droplets from an edge into the other phase. Droplets separated from the surface are size distributed according to the Rosin-Rammler distribution [4].

2.1.9.2 Wave stripping

External forces such as shear or gravity at the interface between the fluid film and the surrounding gas can affect the film surface, so that it develops instabilities leading to droplets leaving the film. The so called wave stripping from the surface happens in a three-stage process. Waves start to develop on the interface between the fluid film and the gas phase. As the film thickness get larger, the waves grow bigger and become unstable and form cylinders (as a results of Kelvin-Helmholtz instability) that are ejected from the film to the surrounding air. The cylinder is then broken up in spherical droplets due to Rayleigh-Taylor instabilities. The surface stripping is characterized as a function of wavelength. Closing the stripping model is done by computing the wavelength where breakup is most likely to occur. The computed wavelength is then the most unstable and can be calculated using the dispersion equation:

$$\lambda_r = \frac{2\pi}{\rho_f \mathbf{f}_b \cdot \mathbf{n}} \left(\frac{1}{3}\rho \tilde{\mathbf{v}}_r^2 - \sqrt{\left(\frac{1}{3}\rho \tilde{\mathbf{v}}_r^2\right)^2 - \rho_f \mathbf{f}_b \cdot \mathbf{n}\sigma} \right) \tag{2.15}$$

where $\mathbf{f}_b$ is a body force acting on a film, $\tilde{\mathbf{v}}_r$ is the relative velocity between fluid film and the surrounding air, and σ is the surface tension. From this the minimum film thickness for droplet ejection can be calculated as:

$$h_{min} = c_H \frac{\lambda_r}{2\pi} \tag{2.16}$$

where c_H is a coefficient for minimum film thickness to initiate stripping [4].

2.2 Eulerian-Eulerian modeling

In the Eulerian-Eulerian model, also known as multi-fluid or two-fluid model, both phase are modeled as Eulerian phases. Droplets and particles can be modeled using the Eulerian model by assuming that the properties of the particle are continuous like a fluid. Particles are then treated as a cloud, represented as an Eulerian field. If the flow is dense (particle-particle collision responsible for particle motion) the collision of particles transfer information in all directions and the particle cloud can be modeled as a continuous fluid. The exchange of mass, momentum and energy between the phases is done through source terms at the interface between the two phases.

The equations for the mass, momentum and energy are developed at a point in the cloud. For each node in the field, the differential conservation equation are discretized and solved using the same methods as for the surrounding fluid. This results in a set of algebraic equations giving the properties of the cloud. The kinetic theory specified for the molecular level of gases have been used to develop the constitutive equation for the particle cloud [5].

In Star-CCM+, the dispersed multiphase model is an Eulerian multiphase model typically used instead of the Lagrangian model. Compared to the Lagrangian model the dispersed multiphase model is much less computationally expensive. The transport equations for conservation of mass and momentum is solved for each dispersed phase. Unlike the Eulerian multiphase model the dispersed multiphase model is one-way coupled by default, thus only solves for the dispersed phase while the background phase is controlled by a single phase solver [4].

2.3 Volume of Fluid

The volume of fluid (VOF) is an interface tracking method. The interface is tracked by defining a function F. When a fluid occupies a point the value of F is unity, otherwise the value is zero. The value is averaged in a cell, whereas the averaged value of F represents the fractional amount of fluid in a cell. Where unity is fluid and zero is lack of fluid.

Cells with a value between unity and zero is then containing a free surface. Afterwards the interface is captured implicitly through the domain. This done with a function that describe the advection of volume fraction of fluid.

$$\frac{d\alpha}{dt} + U_j \frac{d\alpha}{dx_j} = 0 \tag{2.17}$$

When using the VOF method the interface can become smeared and diffusive due to the lower order schemes such as the first order upwind. This is resolved by introducing advection schemes to keep the interface sharp and to give monotonic profiles to the color function.

The fluid flow is computed by solving the Navier-Stokes equations. By weighting the fraction of the two phases one set of equations is enough for the continuity and momentum equations.

2.4 Lattice Boltzmann Methods

Unlike the previous continuum-based CFD methods mentioned above the lattice Boltzmann method originates from the discrete kinetic theory. The main variable of interest in the kinetic theory is the one-particle probability distribution function (PPDF). To derive the Boltzmann equation from the PPDF two assumptions needs to be made:

- No correlation between the velocity and position of the molecule (molecular chaos)
- Only binary collisions are considered.[12]

The Lattice Boltzmann method is modelled in the meso-scale unlike the conventional CFD method, which act on the microscopic scale. I.e. at the macroscopic scale, the Lattice Boltzmann method is able to recover the Navier-Stokes equations [13].

3

Methods

In this chapter, the complete methodology for running the Eulerian-Lagrangian simulation will be presented. This will be followed by a description of the test case on which this methodology is applied. The conclusions taken from this will be applied to the full vehicle geometry.

3.1 Preprocessing

The pre-processing software ANSA from BETA CAE Systems was used for cleaning up the CAD geometry. Surface meshing, volume meshing, flow simulations and post processing was done using Star-CCM+ version 11.06 from CD-Adapco. The CAD was first imported into ANSA and the geometry was split into PIDs. This was done to ease the meshing in Star-CCM+ and in order to create appropriate interfaces for the fluid film modeling (see Section 2.1.9) and to apply boundary conditions easily.

3.1.1 Meshing

Whenever a vehicle geometry is imported into a CFD software, the CAD usually contains open holes, disconnected and overlapping surfaces etc, which might create a problem while creating the mesh. ANSA can be used to clean the geometry, but can be time consuming. Instead, the surface wrapping feature of Star-CCM+ was utilized. It wraps the geometry on a triangulated mesh with a user defined level of detail and removes the CAD problems. The surface wrapper is then remeshed with the surface remesher to create a high quality triangulated mesh which creates a surface suitable for volume meshing [4]. The trimmed cell mesher [4] is used for creating the volumetric mesh. It creates a hexahedral mesh around the surface mesh. Prism layers are used in the near wall region in order to use wall functions to resolve the boundary layer. Details of the case study about meshing can be found in Section 4.1.

3.1.2 DrivAer Model Geometry

A test case study was conducted on a simplified geometry in order to understand the underlying physics of the problem. At the same time, the aim was also to perform a parameter sensitivity analysis and develop a methodology for best practice and balancing accuracy and computational cost. A simplified geometry meant that the simulation times were relatively small. This allowed for faster understanding of the results. The aim of the test case was to figure out which models, and their corresponding parameters, are necessary to make the multiphase contamination simulation resemble real life soiling of a vehicle. To do this on a full car model would not be computationally feasible. The main focus of this thesis is the soiling due to the rear view mirror on the driver side window. Hence, the simplified geometry consisted of only two parts, the mirror and its components, and a wall that represents the driver window (see Figure[3.1]). This geometrical simplification is suitable in this case since only contamination from the mirror to the window is considered. The mirror geometry used for the test case is taken from the generic car model, the DrivAer model. The DrivAer model is a car model developed at the Institute of Aerodynamics and Fluid Mechanics at the Technische Universität München to facilitate aerodynamic investigations of passenger vehicles [3].

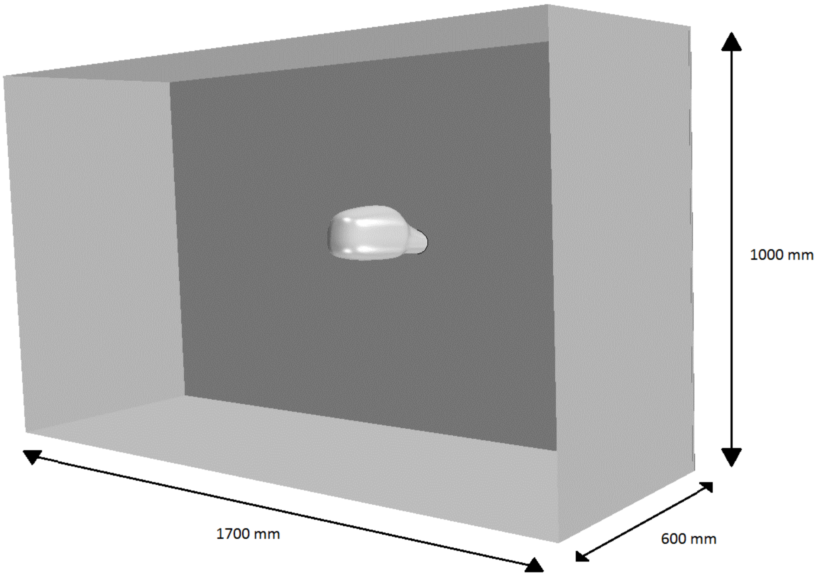

Figure 3.1: The test case geometry

3.2 Parameter Study

There are various parameters governing the flow of droplets and formation of film on the vehicle. First, the flow of air around the vehicle geometry needs to be modeled. A continuum approach using the Eulerian frame of reference was used. The mesh is quite crucial as there needs to be a balance between resolving the flow field correctly while at the same time solving for the Lagrangian phase accurately (see Section 2). For modeling the rain droplets, an injector needs to be used. The properties of the droplets are governed by their size, velocity, mass flow rate etc. Getting the injector to behave close to the real phenomena is important. The flow of the injected droplets is governed by the physics of the coupling between the phases. Particle forces, turbulent dispersion, wall interactions are needed to be modeled. The impingement of droplets on the wall, the formation of fluid film and the shear driven movement of the film on the surface of the vehicle is also to be considered. The separation of film due to edge and wave stripping (see Section 2.1.9.1 and Section 2.1.9.2) affects the contamination on the driver window. The stripping is dependent on various parameters. A study needs to be done in order to determine how the relevant parameters (Section 2.1.9.1) affect the results. The parameters will be analyzed individually to see their effect. Only the most important parameters which are expected to affect the results the most will be analyzed.

3.2.1 Droplet Injector

The droplet size distribution (DSD) depends on the intensity of the falling rain. Rain is classified as light ($I_u \leq 2.5 mm/h$), moderate ($2.5 < I_u \leq 7.6 mm/h$) or heavy ($I_u > 7.6 mm/h$), depending on I_u, the rainfall intensity [2]. In order to model the rain accurately, the correct droplet sizes must be selected. However, selecting a DSD increases the complexity by introducing different length scales in the problem. To simplify the test case, only a constant droplet diameter was selected. For moderate rain, a mean diameter of 0.8 mm [16] is used for the test case.

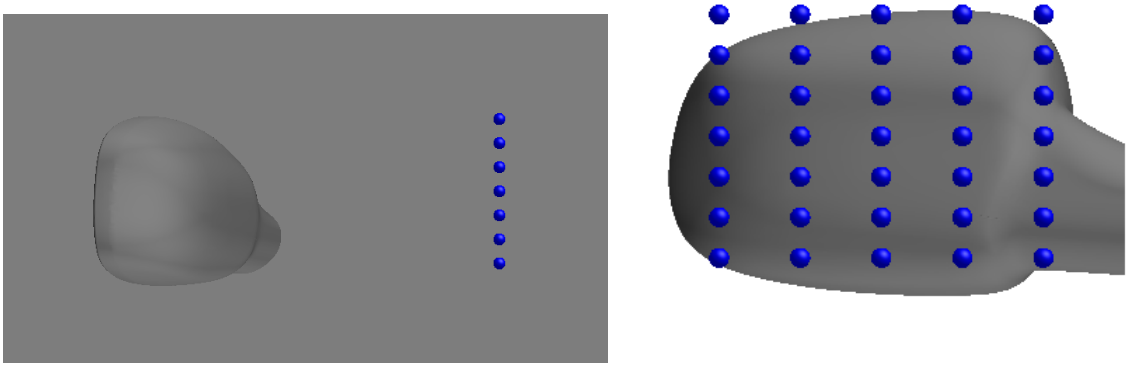

(a) Distance between injection points and the mirror

(b) Distribution of injection points

Figure 3.2: Injection points

Rain droplets are introduced into the domain through an injector. In order to distribute the impingement of droplets and to avoid patchy impingement of droplets across the mirror, a table injector is used [4]. The table injector consists of 35 injection points with an equal distance distribution between the points. The injection points are located near the mirror geometry to reduce the time it takes for the droplets to impact, (see Figure[3.2]), while at the same time have enough distance to get entrained in the flow. Droplets are injected with a total mass flow rate of 0.08 kg/s. The mass flow rate is calculated based on the specifications of the nozzles used in the wind tunnel experiments [17]. It is assumed that the rain droplets are falling at their terminal velocity with a trajectory normal to the ground. However, when the relative velocity of the droplets with respect to the vehicle is calculated, the trajectory is almost horizontal to the ground. This is the reason for having the seeding velocity for the droplets in the horizontal direction. The injection velocity is the same as that of the free stream velocity. One *parcel stream S* is used i.e. each injection point injects one parcel per time-step. The number of particles per parcel N_p are calculated as $N_p = \dot{m}\Delta t/\rho_p I S$, where $\dot{m}$ is the mass flow rate, Δt is the time step, ρ_p is the droplet density, I is the number of injection points and S is the number of parcel streams. With a time step of 10^{-4} s, (see Section 3.2.2) $N_p \approx 1$. However, upon impingement and and stripping, the number of physical droplets increase which increases N_p.

3.2.2 Test Case Setup

Before introducing the droplets into the continuous phase (surrounding air), a steady state simulation is solved for the continuous phase using RANS equations. The pressure-based segregated SIMPLE algorithm is used for pressure-correlation equation calculation. The $k - \omega$ turbulence model with an all y^+ wall treatment is used in the simulations. A constant density is assumed. The converged steady solution is used as an initialization for the two phase simulations.

As mentioned earlier, the test case geometry was chosen to minimize simulation time (see Figure [3.1]).According to the contamination test done previously at NEVS [17], the most amount of contamination on the driver's side window was observed at a velocity of 50 kmph. This was the velocity chosen for the simulation. Time discretization was done implicitly with first order accuracy and an Eulerian time step of 10^{-4} seconds. The size of the time step is small enough for a particle to travel a distance much less than one cell each time step. Hence, the time step needs to be reduced if the simulation is done at higher velocities. 5 inner iterations were done for each transient time step in order to reduce the computational time. The Lagrangian solver is updated once every Eulerian time step. The Lagrangian sub-steps is the number of times each parcel position is tracked during each time step. The maximum number of sub-steps must not be too high, otherwise some parcels might be tracked indefinitely. For the test case, a maximum of 50 sub-steps were specified. 100% of the parcels reached the maximum number of sub-steps for the test case since the geometry is small. For the full vehicle model, a maximum of 200 sub-steps were specified and the number of sub-steps were continuously monitored and sub-stepping was stopped when 30% of the parcels reach maximum number of sub-steps to avoid tracking problematic parcels. In Ref.[23], it was seen that the results does not change after around 30% of the parcels had reached the maximum time steps.

3.2.2.1 Lagrangian Solver

The droplets are modeled using the Lagrangian specification with discrete parcels representing the droplets. The properties of the droplet change as a function of time and space due to the forces acting. The droplet trajectories are calculated with a frozen flow field, while the velocity and position are solved for using Equation 2.1 and the equation:

$$\frac{d\boldsymbol{r}_p}{dt} = \boldsymbol{u}_p \tag{3.1}$$

The same integration is done for all particles in the parcel, and the exchange with the continunous phase is multiplied by the number of particles that the parcel represents [4].

Two-way momentum coupling between the phases is implemented. For a multiphase flow simulation, the boundary between dilute and dense dispersed flows is usually at a volume fraction of the dispersed phase of 10^{-3} [5]. However for contamination simulations, the volume fraction of the droplets can reach up to 10^{-2} [2], which is much higher than

than 10^{-6}, the limit for considering one-way coupling. Also, when film breakup takes place, there might be large quantities of water that are released from the film. This can effect the aerodynamic field around the geometry. Additionally, coupling becomes more important for lower Stokes numbers (see Figure[4.19b], from the full vehicle simulations from Chapter 4) [5]. Hence, two way coupling between the phases is considered. One disadvantage of using two-way couppling is the higher simulation time. Droplet-droplet interaction (four way coupling) is not considered. Even for a high rainfall intensities and large raindrop diameter ($\approx$ 4mm), the mean separation between raindrops is of the order of 70 mm [21] which is much higher compared to the droplet diameter. Consequently, it is assumed that the droplets do not influence each other and do not collide.

The Schiller-Naumann drag coefficient (Equation[2.5]) is used to model the droplet drag force. This coefficient works well for water droplets having $Re_p < 800$. Figure[4.19a] shows the distribution of Re_p for the droplets from the full car simulation (see Chapter 4). It can be seen that all droplets have $Re_p < 800$. The density ratio of the droplets to air is $\rho_c/\rho_p \approx 0.001$, hence the force due to buoyancy, lift force and the virtual mass force have been neglected. The lift force however can be non-negligible in the near wall region for large droplets [22]. The history force is due to unsteady effects and it contains an accumulated integral. It is computationally expensive and is not available in Star-CCM+ [4].

The Bai-Gosman wall impingement model was used to model the interaction between the rain droplets and the vehicle surface. The post impingement characteristics were calculated based on the incident We of the droplets and whether the wall is wet or dry. Fluid film boundaries are considered wet in Star-CCM+ if the fluid film thickness is greater than zero [4].

As mentioned in Section [2.1.7], aerodynamic breakup of droplets depends on the We. Figure[4.19c] shows the distribution of We for the full car simulation (see Chapter 4). It is seen that $We < 12$ for all droplets hence droplet breakup and distortion has not been considered.

3.2.2.2 Boundary Conditions

The inlet is modeled as a velocity inlet with a velocity of 50 kmph or 13.88 m/s. The outlet is a pressure outlet with an atmospheric pressure. The mirror geometry and the wall are fluid film boundaries, while the rest of the boundaries are given symmetry boundary conditions. In the full vehicle case, the whole vehicle surface is modeled as a fluid film boundary. For the Lagrangian phase, all boundaries except the fluid film boundaries were modeled as "escape". That is, the droplets that reaches any of these boundaries are taken away form the domain.

3.2.3 Test Parameters

In order to understand how each parameter is affecting the deposition of film downstream of the mirror, each parameter was implemented and compared one by one. The volume mesh as well as the surface mesh affect the droplet behavior and subsequent fluid film formation and its separation. Different meshes were compared on the test case. The effect of the turbulent dispersion, edge stripping and wave stripping on the film dynamics downstream of the mirror were investigated.

The wall wetting w is defined as $w = h_f A_c \rho$ where h_f is the fluid film thickness, A_c is the surface area of the cell and ρ is the density. Wall wetting essentially quantifies the amount of accumulated film mass on the surface. To compare results, the wall wetting for different cases was analyzed. The contours of fluid film thickness gave an understanding of how much contamination due to the rain droplets was occurring. The mass flow rate of droplets at the outlet was studied to quantify the amount of stripped droplets from the mirror that reaches the outlet.

Simulations were performed on a simplified geometry to analyze the sensitivity of formation of fluid film in the wake of the generic mirror on various parameters. The idea was to find best practice methodologies in order to get a good compromise between having an accurate solution and a reasonable computational cost. As mentioned earlier, it would be impractical to run this analysis on the full geometry.

3.3 Experimental technique

The experiments were performed at NEVS climate tunnel facility on a NEVS 9-3 car. Two different mirror designs were tested during a rainy condition in the tunnel. The mirrors were 3D printed and mounted on the vehicle. A water and fluorescent particle mixture was used to make the droplets visible on the car exterior. Water droplets were injected through 4 nozzles, mounted on a square steel frame with the dimensions of 250x250 mm. The injectors were located 1.6 m from the car wheel center and placed right in front the mirror. The droplets, injected with a pressure of 4 bar, were carried by the wind entering the domain with a velocity of 50 kmph. UV-lights were used to follow and see the droplets sticking, stripping and forming film on the exterior of the car. The documentation of the results was done by filming and taking pictures during and after the experiment. These pictures and movies were later compared with the post-processed results from the simulations. Only qualitative data could be obtained from the experiments performed.

3.4 NEVS 9-3 Simulation

The conclusions and results from the test case were implemented on the NEVS 9-3 vehicle model. A half model of the car, divided in the middle, was placed in the domain shown in Figure[3.3]. All the surfaces except for the inlet (in front of the car bumper), outlet and the ground (below the wheels) have the boundary condition symmetry, see Table 3.1. For the injector, the same settings were used as in the test case for the half car simulation. In order to keep the number of cells in the domain low, the size of the virtual wind tunnel was kept small. The largest reduction was done in the wake region of the car since the wake characteristics of the flow are not a primary interest. The single phase steady state RANS solution was used as an initial condition for the transient unsteady case.

Table 3.1: Boundary Conditions

Inlet	Velocity Inlet - 50 kmph
Outlet	Pressure Outlet - Atmospheric
Roof	Symmetry
Floor	Wall with free stream velocity
Body	Wall with zero velocity
Symmetry Plane	Symmetry

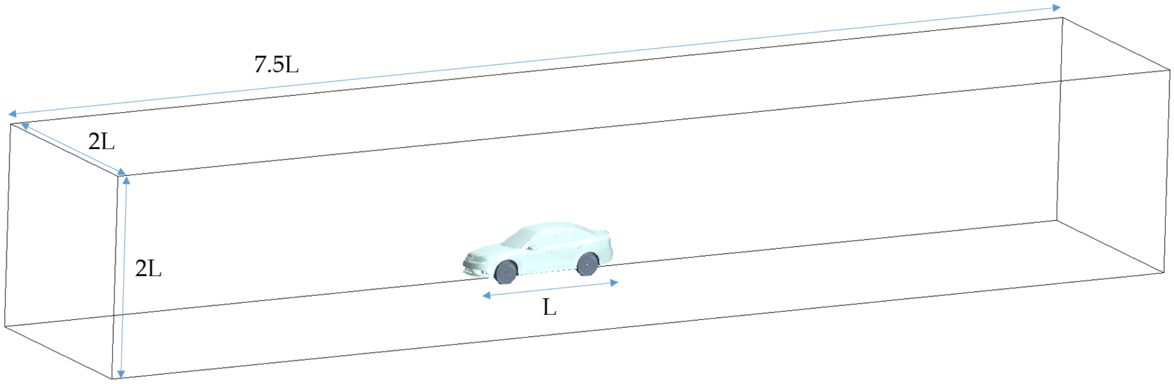

Figure 3.3: Computational Domain

For the Lagrangian parcels, the vehicle surface is treated as a wall and at the rest of the boundaries, the Lagrangian parcels escape from the simulation. On the left side of the car the wall surfaces, window, door and mirror, are modelled as a fluid film boundary condition.

4

Results and discussion

This chapter will present the results from the test case study and the NEVS 9-3 simulations. The NEVS 9-3 simulations will also be compared with the experimental tests conducted.

4.1 Test Case Findings

The parameters discussed in Section 3.2.3 determine the flow of droplets and film over the mirror and the driver window.

4.1.1 Sensitivity to volume mesh

The geometry and domain described in Section 3.1.2 earlier was meshed using semi structured, trimmed hexahedral cells. The meshing tool in Star-CCM+ was utilized for this [4]. The aim of this study was to identify how important it is to resolve the turbulence in the boundary layer relative to predicting the fluid film dynamics accurately. The resolution of the boundary layer depends on how small the height of the first cell in the domain was and the dimensionless wall distance y^+. Since the point source approximation[5] is used for the Lagrangian droplets, the volume fraction of the droplets must not be too high in any discretized cell of the continuum phase. Hence, a balance needs to be found between solving the flow field accurately and resolving the Lagrangian dynamics correctly. The resolution of the boundary layer was varied by changing the prism layer thickness and consequently the y^+. Table 4.1 depicts the different meshes studied.

1st cell height(mm)	**Average y_+**	**Cell Count**	**Number of prism layers**	**Prism layer Thickness(mm)**
0.1	2	600000	8	4.93
0.3	5	580000	5	2.23
0.8	15	498000	4	4.29
2	45	390000	3	7.28

Table 4.1: Volume mesh

One of the main assumptions of Eulerian-Lagrangian modeling is that of dilute flow i.e. small volume fraction of the Lagrangian parcels. However, when droplets are impinging on the solid surface, the volume fraction can increase by an order of magnitude due to the small cell size in the near wall region. A volume fraction upper limit of 0.2 was chosen to apply a limitation on the source terms from the droplets to the air [4]. As mentioned earlier in Section 3.2.1, the injected droplets have a diameter of 0.8 mm. For the finer meshes, the droplet size is larger than the height of the first cell. To avoid force integration over multiple cells, Star-CCM+ uses a source smoothing method by which the source terms from the droplets are distributed over many cells.

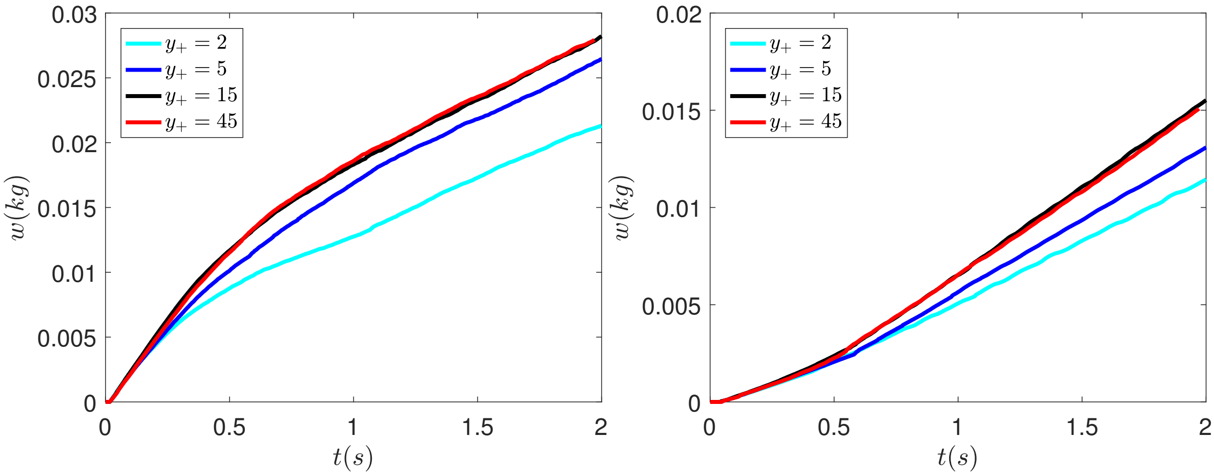

(a) w on enitre domain (b) w on wall

Figure 4.1: Wall wetting

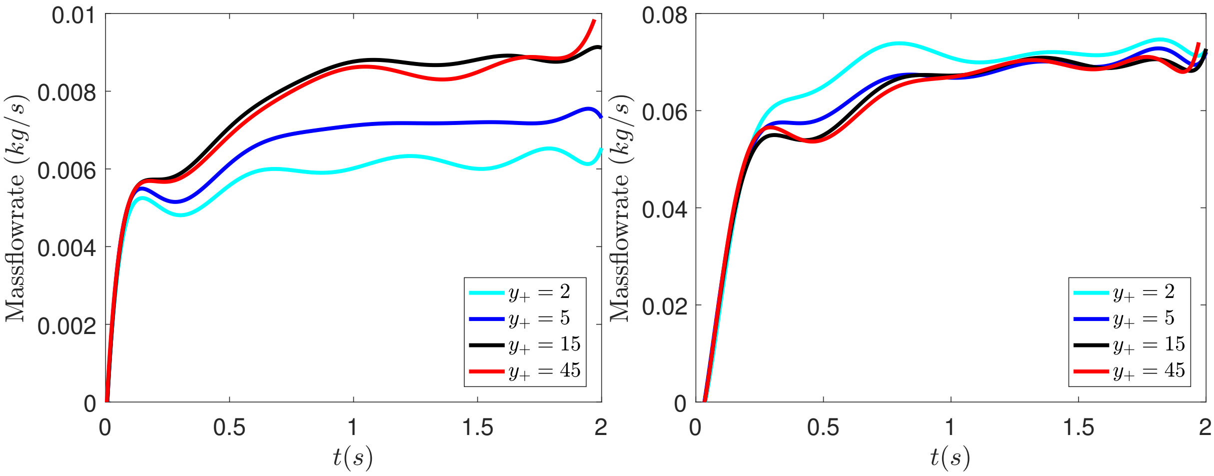

(a) Mass flowrate on wall (b) Mass flowrate at outlet

Figure 4.2: Mass flowrate of droplets

While studying the effects of the volume mesh, the rest of the parameters were kept the same. Figure[4.1] depicts the wall wetting for different y^+ as a function of physical time. It is seen that a mesh having lower y^+ predicts lower wall wetting, both at the wall and the entire domain. As mentioned in Section 2.1.8.1, the equivalent film thickness criterion is used for transition to fluid film. For lower y^+, the droplet-droplet interactions are significant due to the small size of the cells but are not taken into account. Also, the number of droplets in the cell next to the wall are lesser for a finer mesh. Due to this, the criteria for transition to film is not satisfied leading to less film formation. The mass flow rate of droplets impinging on the wall is under-predicted (Figure[4.2a]) for the finer meshes. However, the mass flow rate at the outlet is higher for the finest mesh because lesser droplets are interacting with the the mirror and the walls, leading to less impingement and hence more flow to the outlet (see Figure [4.2b]).

Figure [4.3] shows the contours of fluid film thickness from the underside of the mirror. Much less film formation takes place for the fine mesh. For the $y^+ = 5$ mesh, a region of high film thickness is seen before the edge of the mirror. For the coarse mesh, the film travels to the edge of the mirror and then separates to form droplets. This is similar to the behavior seen in the experiments (see Section 4.2).

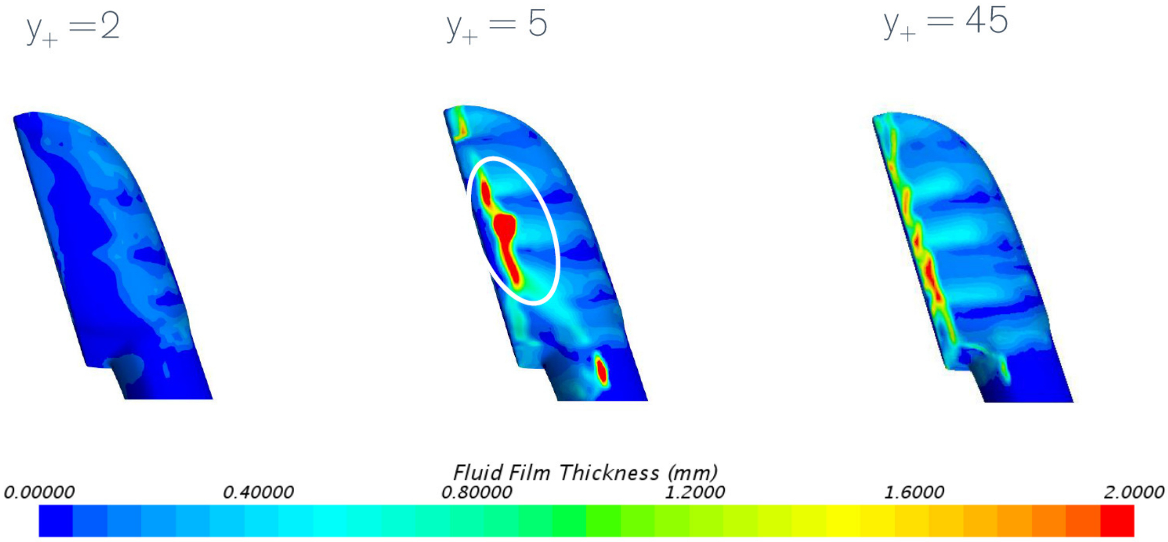

Figure 4.3: Contours of fluid film thickness from underneath the mirror

4.1.2 Sensitivity to surface mesh

To investigate the sensitivity of the surface mesh discretization on the film formation, the resolution of the boundary layer was kept constant ($y^+ = 45$) and the base size of the surface mesh was varied. The same physics was used for all simulations. Three surface cell sizes were investigated, 10mm, 5mm and 2.5mm.

Figure[4.4] depicts the comparison of contours of fluid film thickness on the housing of the rear view mirror. It is seen that film formation is highly dependent on the resolution of the surface mesh. A finer mesh leads to a better resolution of the film formation dynamics. However, the total amount of wall wetting is fairly independent of the surface mesh. This can be clearly seen in Figure[4.5a]. Where, the 10mm cell sized mesh predicts a slightly lower wall wetting (≈ 0.5 g) as compared to the other two surface meshes.

In Figure[4.5b] it is seen that the mass flow rate at the outlet is not affected to a great extent by the resolution of the surface mesh. This is because the mass flow rate at the outlet is dependent on how many new parcels are created because of the separation of film into droplets from the edges of the mirror. The stripping phenomena is more dependent on the volume mesh rather than the surface mesh. Based on these results, it was concluded

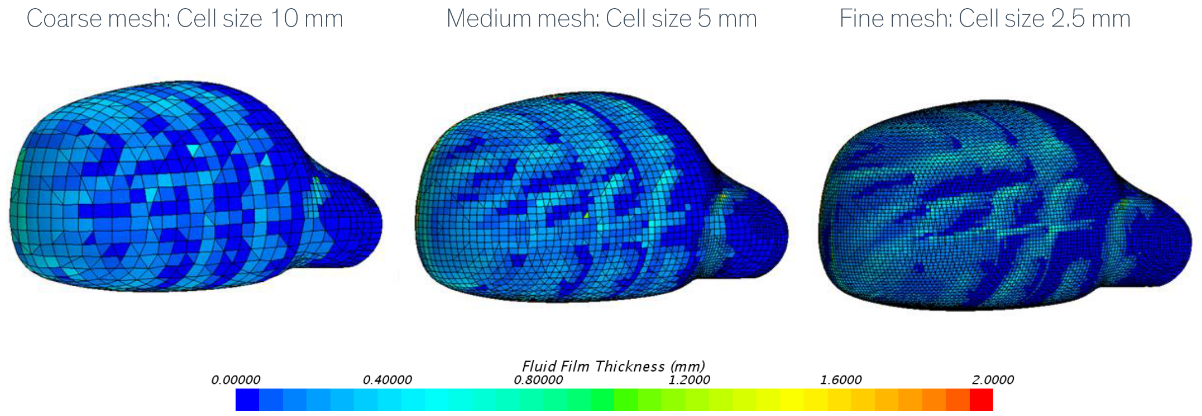

Figure 4.4: Contours of fluid film thickness on mirror housing

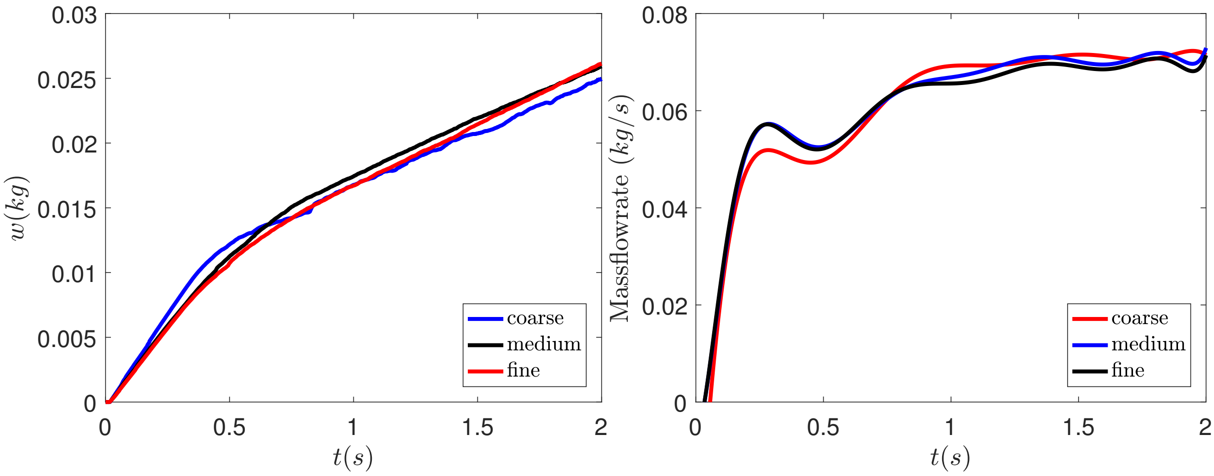

(a) Wall wetting

(b) Mass flowrate at outlet

Figure 4.5: Mass flowrate of droplets

that the refinement of the surface mesh is needed only in areas where resolving the exact behavior of the film was needed to be predicted. The number of cells in the domain could be reduced by having a coarser mesh in areas where only getting the total amount of wall wetting was relevant. For the full car simulation, this meant that the surface mesh needs to be fine on the mirror housing and the driver side window. The rest of the car would have a coarser mesh ($\simeq$ 10mm).

4.1.3 Edge stripping angles

To find a suitable range for the minimum corner angle required to attain film stripping from the mirror edges (see Figure[2.3]), a study on various stripping angles was performed. According to experiments performed by Friedrich et.al [18], a force ratio of 1 predicts the onset of separation of fluid film for free stream velocities below 20 m/s and Re_f below 400. The minimum angle required for stripping to occur decreases with Re_f for a given free stream velocity [18]. The angle between two faces depends on the level of discretization of the surface mesh. If the minimum stripping angle is too low, then film stripping will occur whenever the angle exceeds the specified value thus over predicting the amount of film separation. However, at the same time if the angle is very high, then the film will never satisfy the condition of separation and will recirculate leading to unphysical behavior.

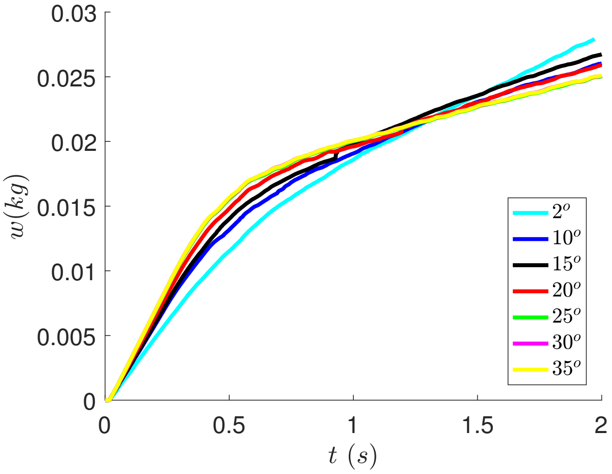

Figure 4.6: Wall Wetting

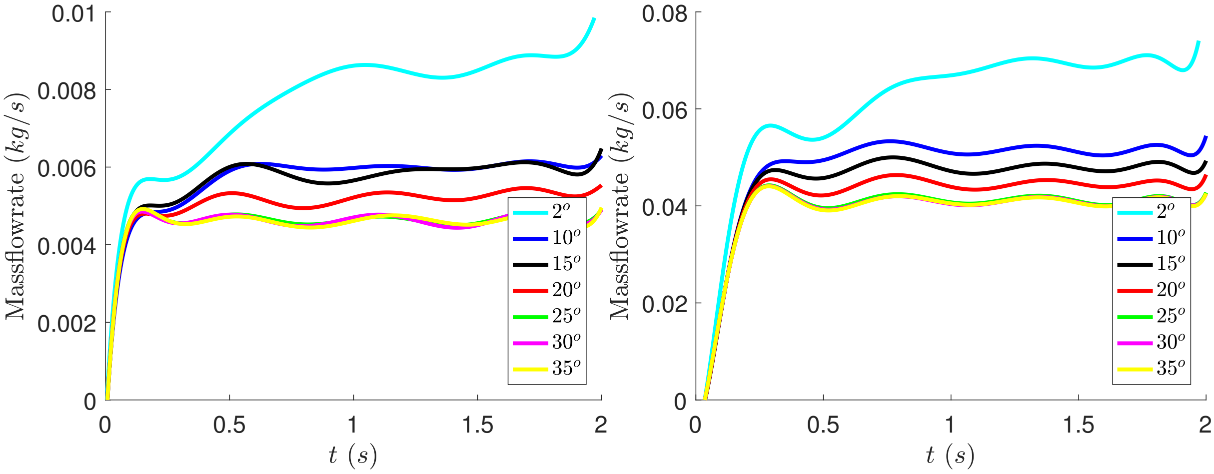

(a) Mass flowrate of droplets at side wall (b) Mass flowrate of droplets at outlet

Figure 4.7: Edge stripping angle

Several different angles between 2° and 65° were tested. The mesh used for these had a y^+ value of 45. The surface mesh was of 5 mm size. Figure[4.6] depicts the wall wetting as a function of physical time for seven different stripping angles. For angles above 25° the plots for the wall wetting as well as the mass flow rate at the outlet coincide (Figure[4.7b]). The lowest angle, 2° has the highest mass flow rate by far at the wall and the outlet. Mass flow rate for minimum stripping angles of 10° and 15° is matching at the wall. This indicates that a similar amount of stripped droplets reaches the wall (see Figure[4.7a]). However, looking at the mass flow rate at the outlet, Figure[4.7b], it is clear that the 10° angle generates more stripped droplets. In the case of wetting on the entire domain the 15° and 20° angles is overlapping while 2° and 10° have a slightly larger wetting.

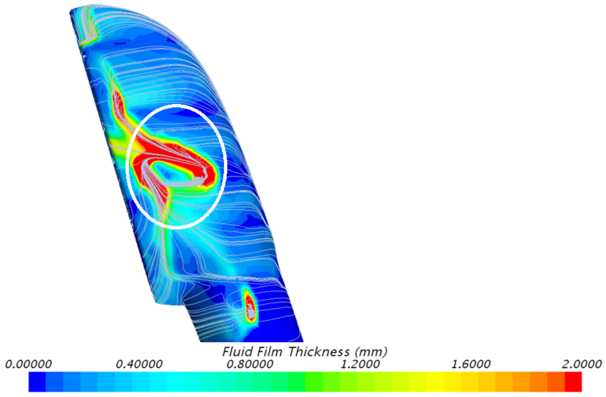

Figure 4.8: Circulation region on mirror for a stripping angle of 25°

Due to the same amount of particles stripping for angles above 25° it is clear that an angle of around 25° is the maximum to attain film stripping. By investigating this closer it is clear that there is no stripping occurring at this this angle and subsequently for higher angles. Instead a recirculation area is appearing on the bottom of the mirror, see streamlines of the fluid film in Figure[4.8], since the condition for film stripping is never being satisfied. This is the reason for the unphysical recirculation zone. For the full car simulations, the minimum edge stripping angle used was 10^o. This angle was chosen since the discretization of the mesh is captured accurately as well as the the recirculation of film is avoided.

4.1.3.1 Additional models

Turbulent dispersion and wave stripping is introduced to the already available edge stripping model. Wave stripping increases the number of particles leaving the mirror housing, this can be seen in Figure[4.9], where the mass flowrate at the outlet is a lot higher for the models including wave stripping. While for the mass flowrate at the wall the simulation including all three models have the highest number of droplets reaching the wall, followed by the edge and wave stripping model. A similar trend can be seen for the he accumulated film mass on the wall (Figure[4.10]), where the simulation including the turbulent dispersion and the stripping models have the highest amount of accumulated film mass. However, the overall prediction of the film mass is almost equally large for all three models.

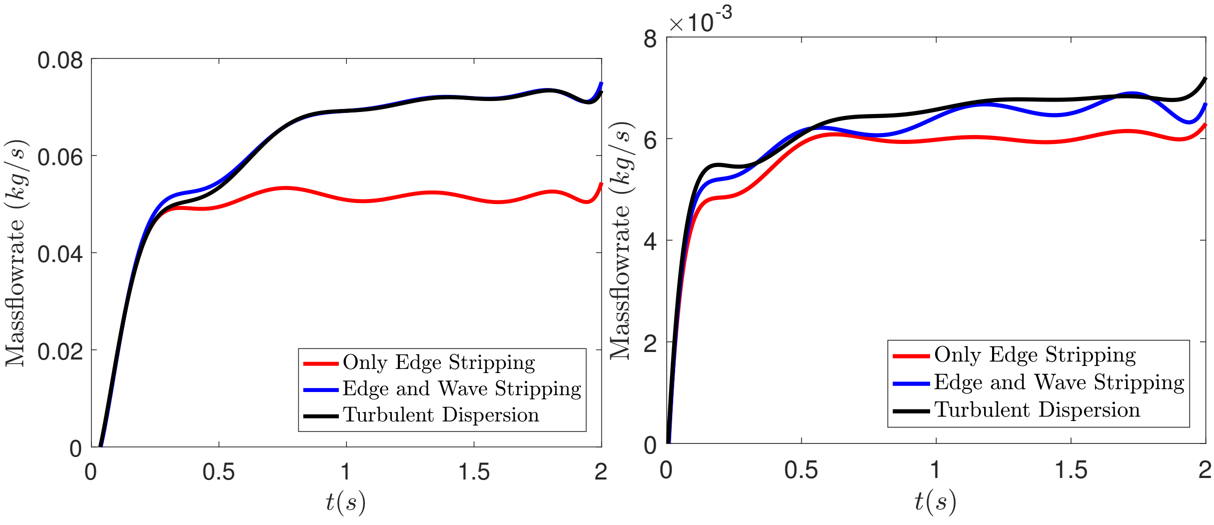

(a) Mass flowrate at the outlet

(b) Mass flowrate at the mirror

Figure 4.9: Mass flowrate of droplets

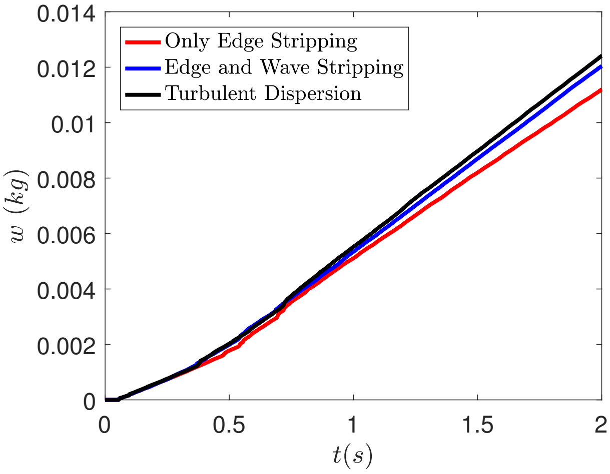

Figure 4.10: Fluid film mass

The distribution of the film on the wall is on the other hand different. The film dynamics downstream is affected by the wave stripping and turbulent dispersion, resulting in less film formation downstream on the wall (Figure[4.11]). While the film formation on the wall directly after the mirror is much larger. To select the one predicting the film more correctly is not possible without comparing with the experimental results.

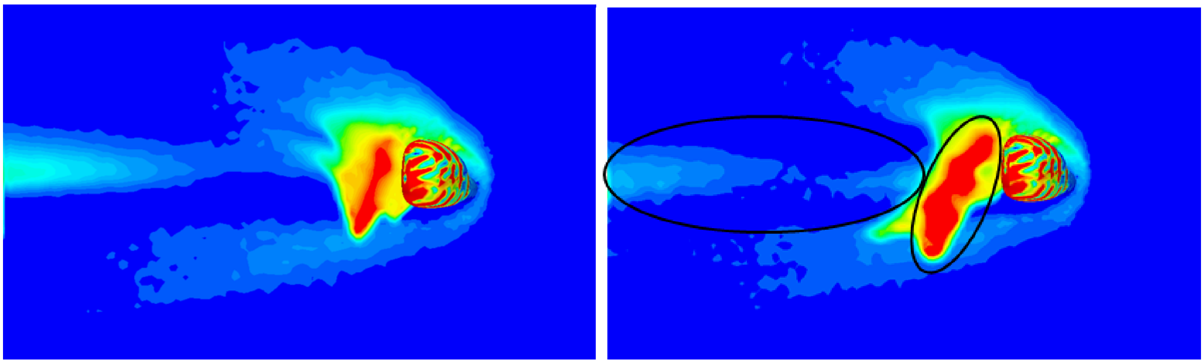

(a) Edge stripping

(b) Turbulent dispersion, edge and wave stripping

Figure 4.11: Fluid film mass on mirror and wall

4.2 Experiments

Two mirror designs were tested in the experiments. The first one was an older NEVS design which was made without a "mudrib". From previous experiments performed at NEVS, it was found that the film which is separated from the underside of the mirror leads to most contamination on the driver side window. In order to reduce this, a "mudrib" was added to the mirror. The mudrib is a protrusion that allows the film to separate from the mirror much before the film reaches the edge of the mirror housing. The two mirrors are shown in Figure[4.12]. The test was conducted at three velocities, 50, 70 and 90 kmph, the results of which are shown in Figures [4.14], [4.15] and [4.15] respectively.

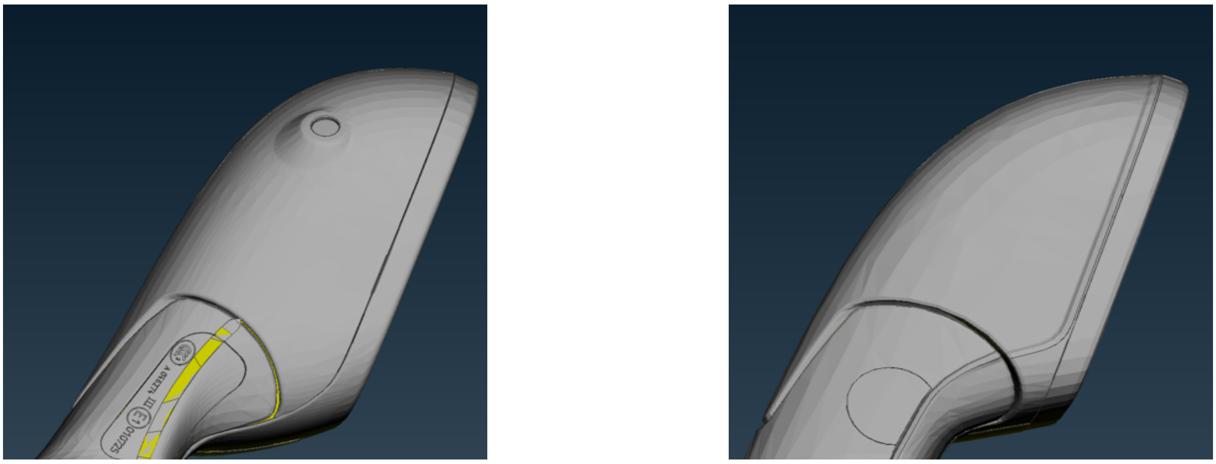

(a) Without Mudrib

(b) With Mudrib

Figure 4.12: Tested Mirror designs (view from underneath)

Figure 4.13: Deposition Regimes [1]

Bannister [1] classified the deposition of droplets into two categories, namely the wake droplet related dirt, which comes from the separated film from the mirror and the fine spray related dirt (see Figure [4.13]). In addition, there is also film which flows down from the A-pillar, named as the A-pillar overflow.

At 50 kmph, the difference between the cleanliness of the driver side window for the two mirror designs is clearly visible. The droplet related wake is reduced in size with the addition of the mudrib. Also, the amount of droplets impinging on the driver side window is reduced considerably. The spray related dirt is predicted similarly for both cases. However, the cleanliness of the mirror glass is not reduced by adding the mudrib at 50 kmph (see Figure[4.14]).

(a) Without Mudrib

(b) With Mudrib

Figure 4.14: Experimental results at 50 kmph

At 70 kmph, similar trends are seen. The spray related dirt predicted is the same for both cases. However, more importantly the droplet related dirt on the driver window is reduced significantly (see Figure[4.15]). A similar prediction is seen on the mirror glass for both with and without the mudrib.

(a) Without Mudrib

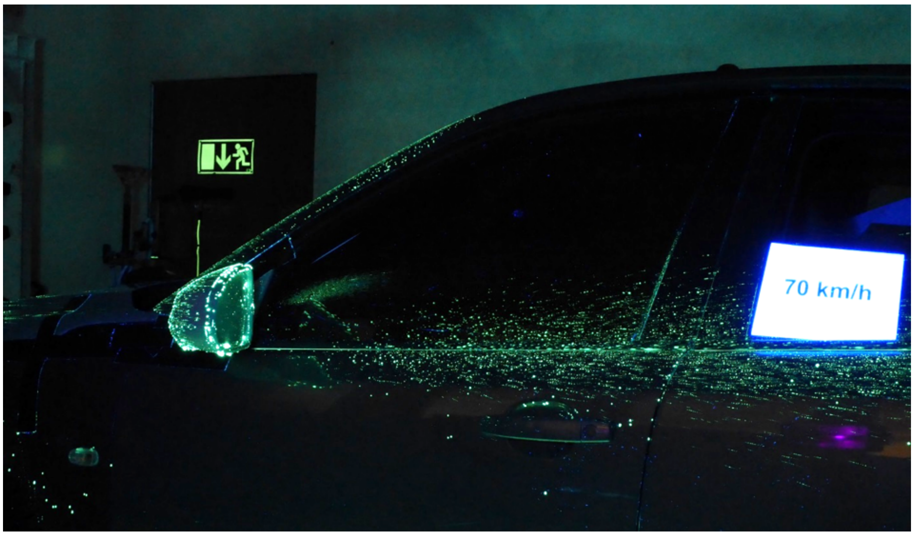

(b) With Mudrib

Figure 4.15: Experimental results at 70 kmph

At 90 kmph, the We number of the droplets increases, leading to aerodynamic breakup, hence much smaller droplets are present in the flow as they are entrained easily in the flow. Once the film is deflected by the mudrib, the droplets take the trajectory of the air and this leads to less impingement on the driver window. The mirror glass is also cleaner with the mudrib at 90 kmph (see FIgure[4.16]).

(a) Without Mudrib

(b) With Mudrib

Figure 4.16: Experimental results at 90 kmph

4.3 Full Vehicle Simulation

The conclusions and results from the test case (Section 4.1) were implemented on the full vehicle, NEVS 9-3 model. Just like the experiments, two mirrors were simulated, with and without the mudrib. An unstructured mesh with trimmed hexahedral cells was constructed. As mentioned in Section 4.1.1, a first cell height of 2 mm with 3 prism layers were used to resolve the boundary layer with a total prism layer thickness of 7.28 mm. A growth ratio of 1.2 was used for the prism layers. The prediction of dynamics of film formation on mirror and the driver window needs to be accurate. Hence a finer mesh is made on those regions with a base size of 5 mm. The rest of the surfaces of the vehicle are meshed with a base size of 25 mm. The mesh in the domain can be seen in Figure[4.17]. The surface mesh around the mirror and the driver window can be seen in Figure[4.18].

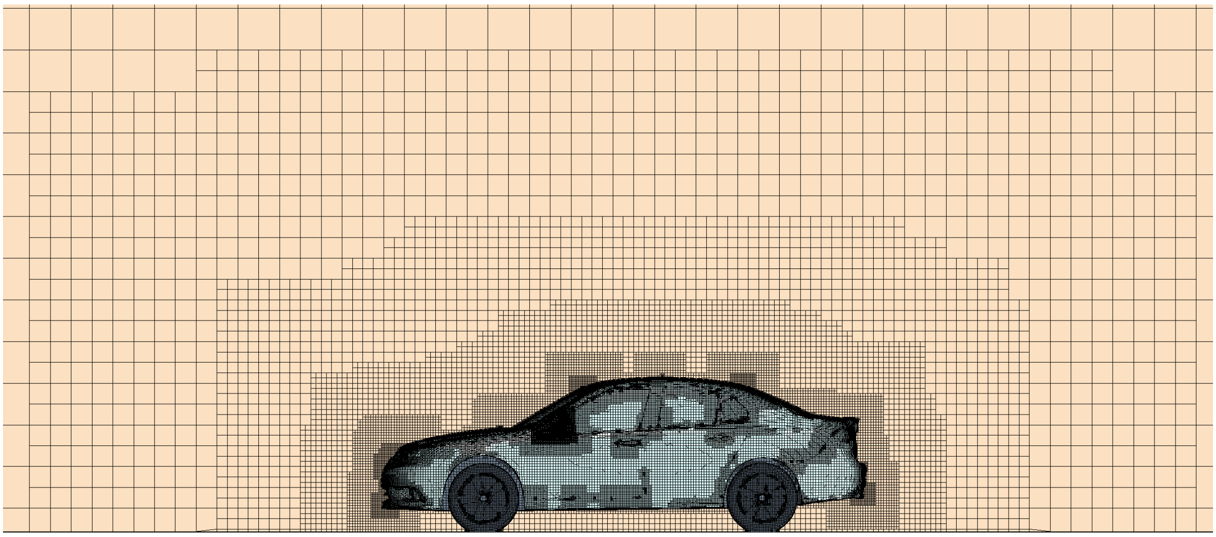

Figure 4.17: Domain Mesh

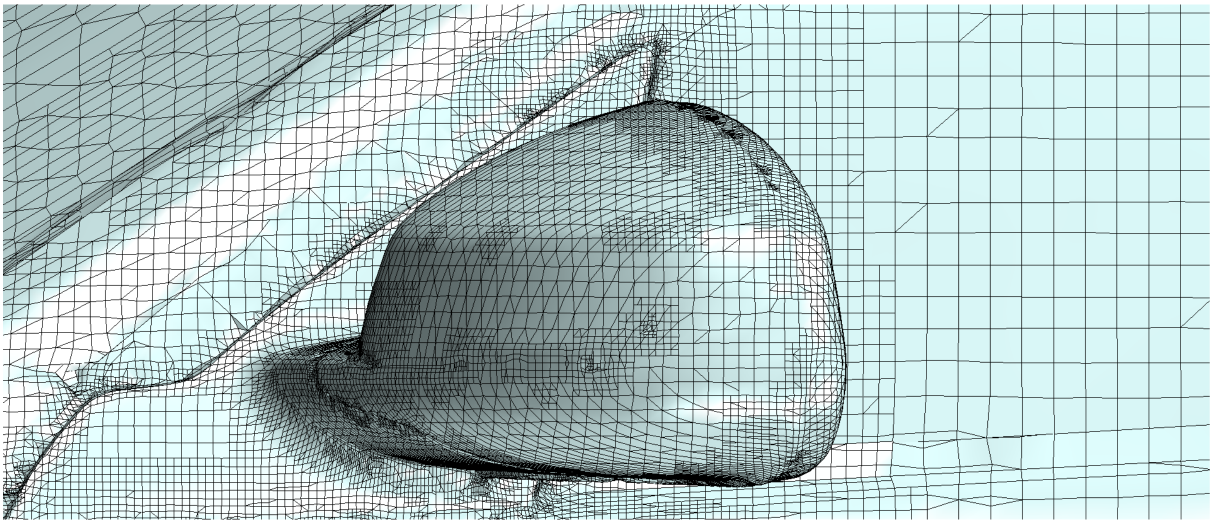

Figure 4.18: Mirror Mesh

The solver settings were kept the same as that of the test case. A total physical time of 1.3 seconds was simulated. The number of Lagrangian sub-steps were continuously monitored and the sub-steps were terminated if more than 30% of the parcels had reached the maximum sub-steps [23]. A minimum edge stripping angle of 10^o was used. The simulations were performed with and withput modeling turbulent dispersion in order to predict the best match to the results. The aerodynamic breakup and distortion of droplets is not modeled (see Section 3.2.2.1). Figures [4.19] and [4.19c] show the distribution of Re_p, St and We on the droplets at a free stream velocity of 50kmph. At higher free stream velocities, the We and Re_p will increase, for which droplet breakup and distortion will have to be considered.

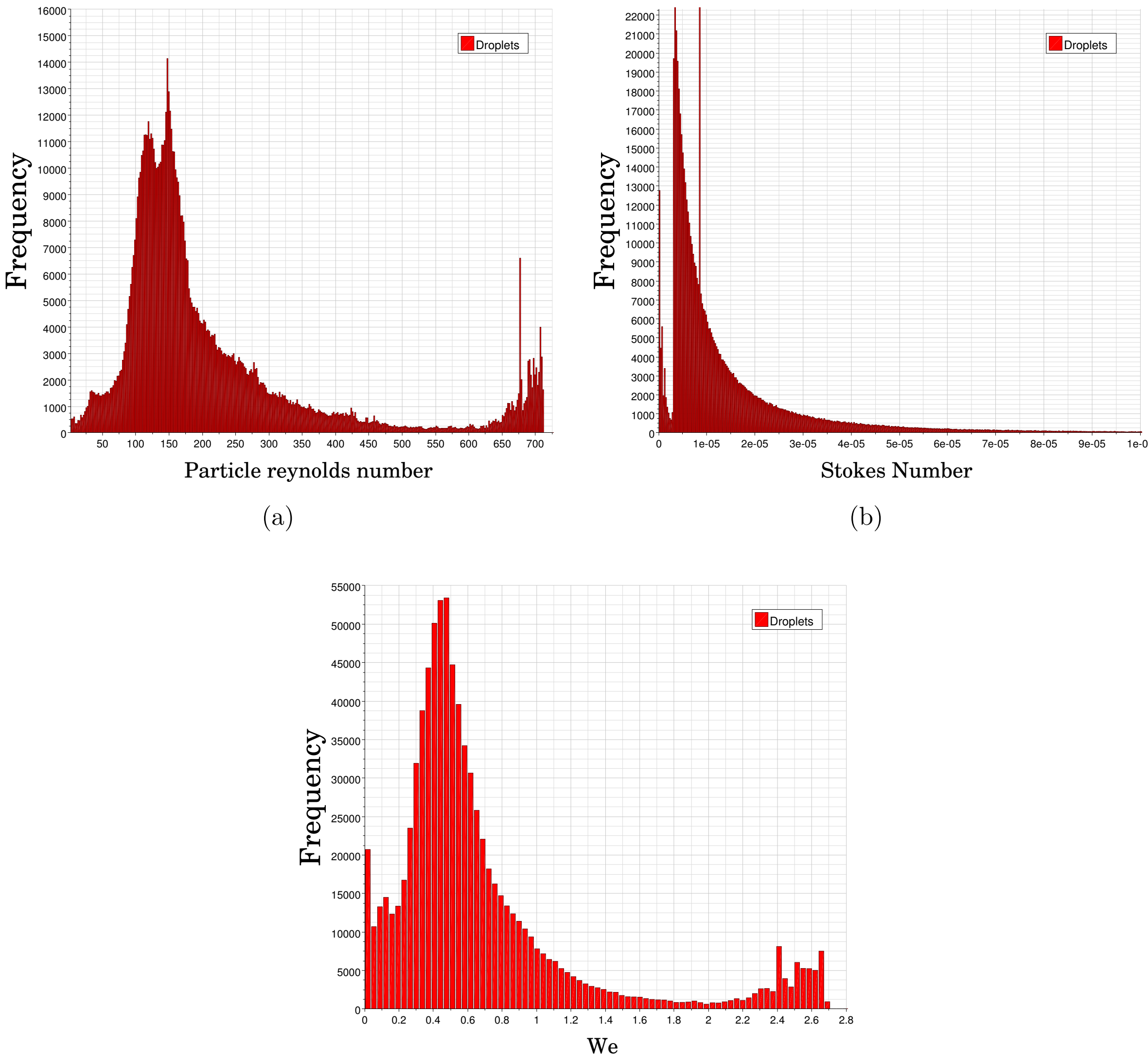

(a)

(b)

(c)

Figure 4.19: Droplet dimensionless numbers

Figure[4.20] shows the plot of velocity on a clip plane passing through the mirror after the steady state solution. Due to the strong two-way coupling, there is a change in the velocity contours. The point of separation of the flow from the mirror is reached much earlier after the flow is coupled. The wake region is becoming bigger due to the ejection of new droplets from the surface of the mirror.

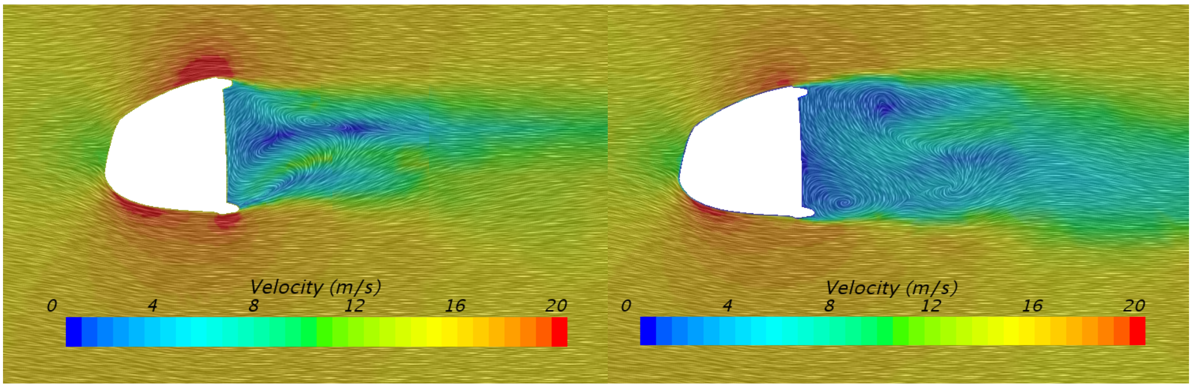

(a) Steady (b) After injection of droplets

Figure 4.20: Line Integral convolution of velocity

It is seen that the injected droplets follow the trajectory of the the aerodynamic flow field before impingement and interacting with the walls. This is because the Stokes number of most droplets is very small (see Figure[4.19b]). Upon impingement on the rear view mirror housing, the droplets convert to fluid film and the film flows to the edges of the mirror housing. Then, the film separates into more droplets which leads to impingement in the driver side window and the doors. Various different regimes of impingement on the surface of the vehicle are observed. The details are presented in the following section.

4.4 Comparison of experiments with simulations

The experimental results have been compared with simulations for both the mirrors, with and without mudrib at 50 kmph. Their comparison with the experimental results will be presented in this section.

4.4.1 No Mudrib Simulation

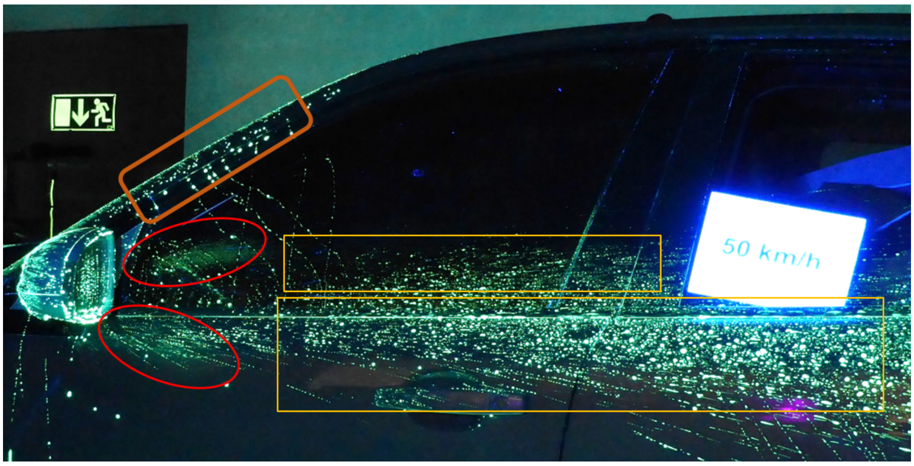

(a) Experiment

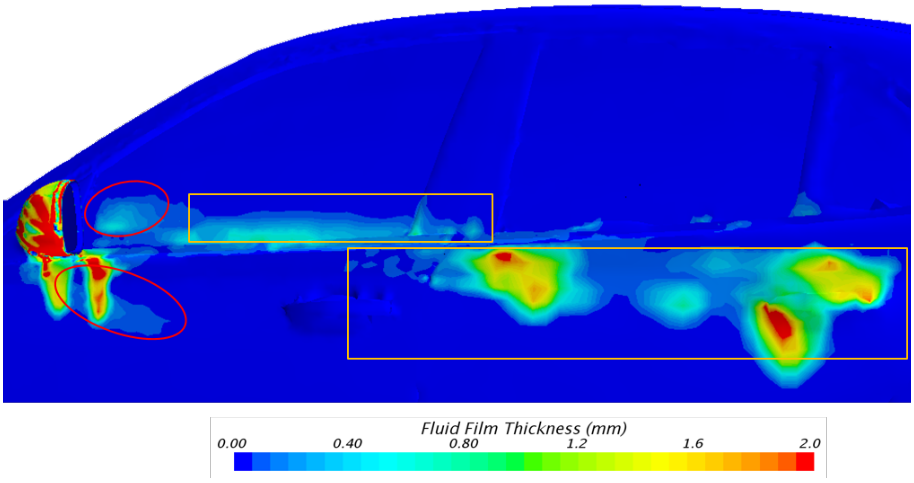

(b) Contours of fluid film thickness

Figure 4.21: Contamination on the side of NEVS 9-3 - no mudrib (experiment v/s simulation)

▭ - A pillar overflow
⬭ - Fine spray related dirt
▭ - Wake droplet related dirt

Looking at Figure[4.21b], it is seen that there is no A-pillar overflow observed. This is because the injection of droplets is only in front of the rear view mirror. In a more realistic simulation, the exact location of rain grid as used in the experiment will be modeled. The fine spray related dirt is predicted similar to the experiment. The wake related droplet dirt is not as much pronounced below the driver window as compared to the experiment. The wake related dirt is pushed further downstream of the driver's side window. However, the contamination predicted in the most crucial area, the driver window is predicted quite similar to the experiment.

4.4.2 Mudrib Simulation

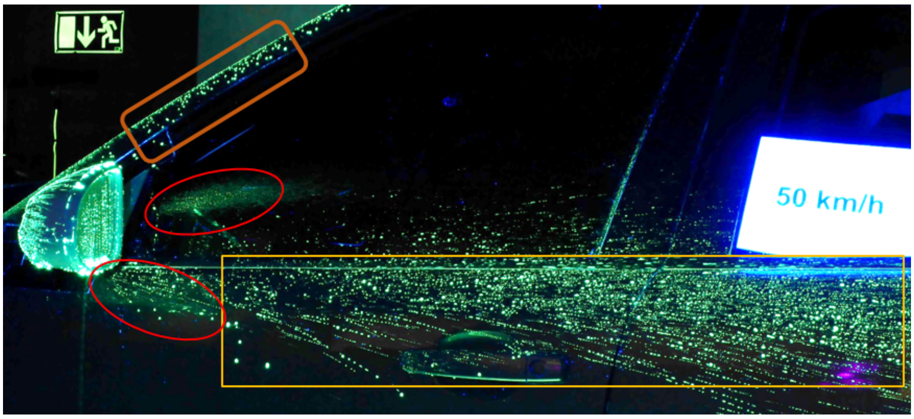

(a) Experiment

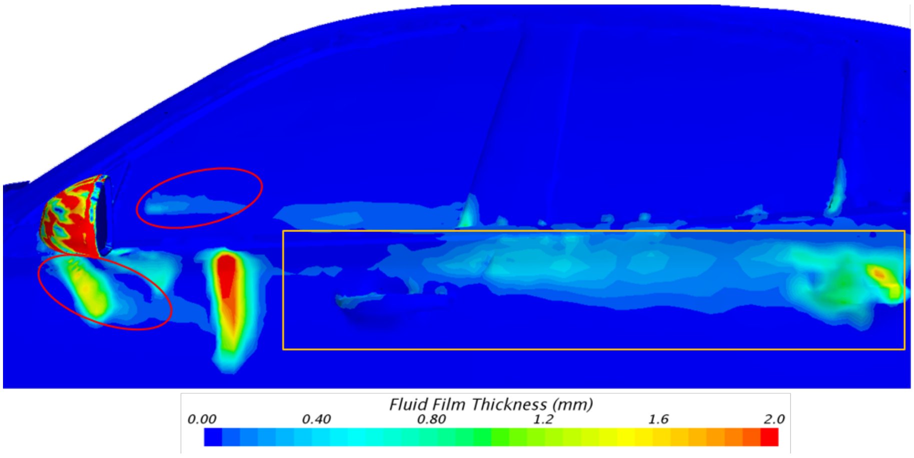

(b) Contours of fluid film thickness

Figure 4.23: Contamination on the side of NEVS 9-3 - mudrib (experiment v/s simulation)

Figure[4.23] compares the experiments to the simulation at 50 kmph for the mirror with mudrib. As before, the spray related dirt is predicted similarly to the experiment. The wake related droplet dirt is pushed further downstream. Most importantly, the pattern of contamination on the driver window is predicted similar to the experiments. Figure[4.24] shows the amount of wall wetting as a function of time for the two cases discussed above.

There is a considerable reduction in the amount of film deposited on the driver window. This can also be seen in Figure[4.25] which shows the the contamination on the driver window for the two mirrors tested. In conclusion, the film deposition on the driver window is similar to what the experiments predict. Table 4.2 shows the mass of fluid film deposited on the driver window and the whole domain for the case with and without mudrib. It is seen that adding the mudrib reduces the contamination on the driver window from 1.15 grams to 0.06 grams.

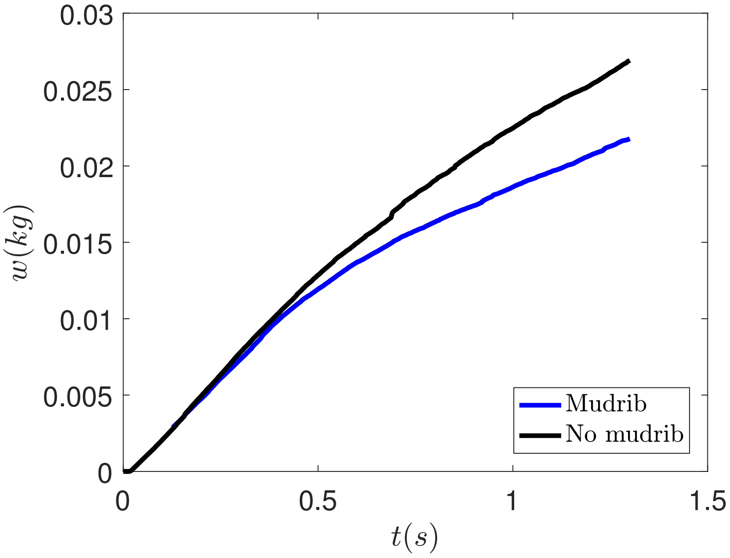

Figure 4.24: Wall wetting comparison - Full car

Figure[4.26] shows the contours of the film Reynolds number Re_f and streamlines of fluid film velocity from underneath the mirror. In Figure[4.26a], the circled regions show where the streamlines end. This is where the fluid film separates to form droplets. It is seen that the separation points of the film are close to the window. The separation is taking place at $Re_f > 300$ as documented in Ref[18]. It can also be observed that the streamlines are coming from the side of the mirror to separate at one location (the upper circled region). This is not seen in Figure[4.26b] where the streamlines do not come from the side of the mirror to the bottom. The film instead separates much earlier (see upper circled region). Also, the film is directed away from the driver window due to the mudrib (see squared region) and hence separates much further away from the window leading to lesser contamination.

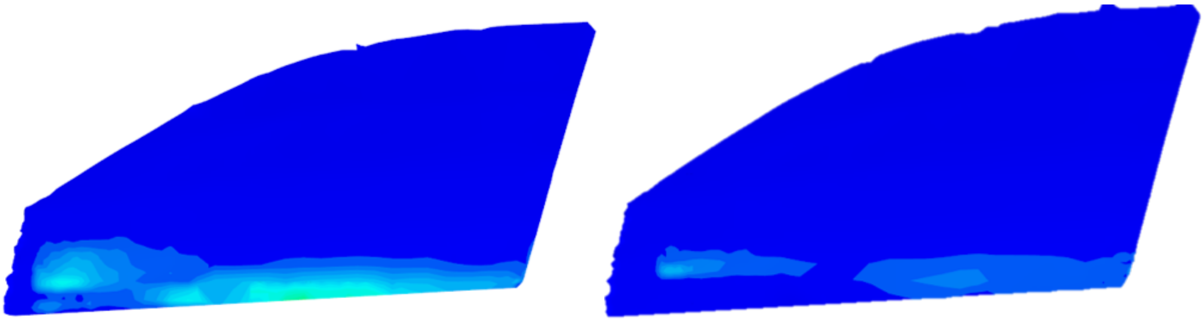

(a) Without Mudrib

(b) With Mudrib

Figure 4.25: Contamination on driver window - comparison, colored from blue to red by h_f, from 0mm to 2mm

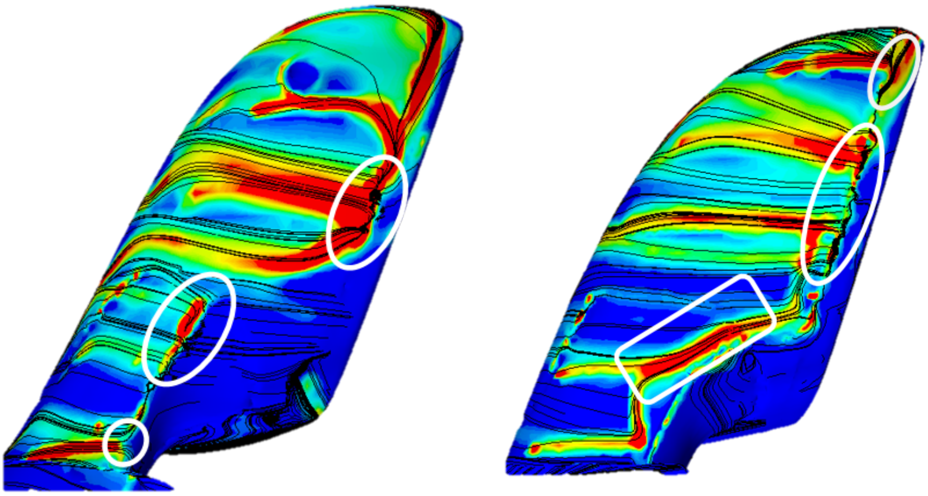

(a) Without Mudrib

(b) With Mudrib

Figure 4.26: Contours of Re_f from underneath the mirror, colored from blue to red by Re_f, from 0 to 300

4.4.3 Turbulent Dispersion

Whether the turbulent dispersion model available in Star-CCM+ was accurate enough could not be determined in the test case simulations. The simulations of the mirror with the midrib were compared by running two cases, with and without modeling turbulent dispersion. Figure[4.27] shows the contours of fluid film thickness on the side of the vehicle. It is seen in Figure[4.27a] that the spray related dirt is not predicted when the turbulent dispersion is modeled. Additionally, the contamination on the driver window is predicted much higher in Figure[4.27a]. Table 4.2 compares the wall wetting on the driver's side window with and without turbulent dispersion. Modeling turbulent dispersion is predicting the film deposition almost five times to that without turbulent dispersion, even though the wake spray related deposition is not seen in Figure[4.27a].

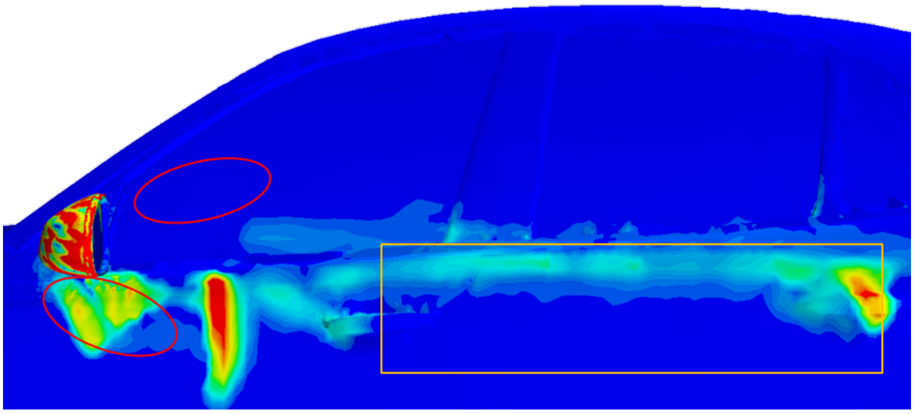

(a) Turbulent Dispersion modeled

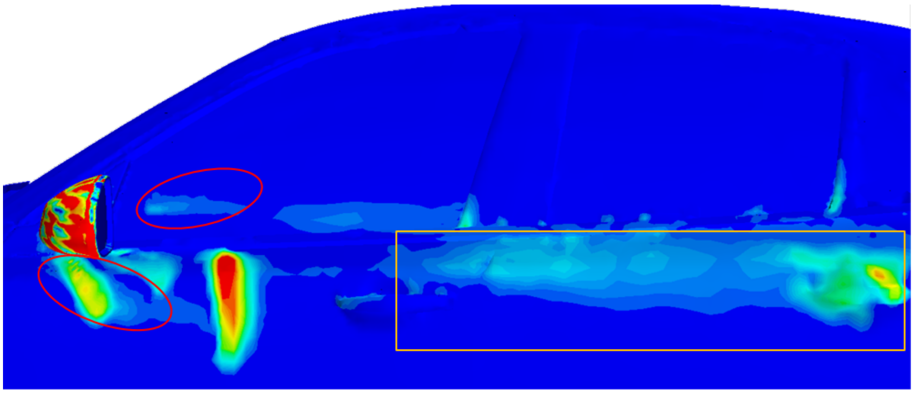

(b) Turbulent Dispersion not modeled

Figure 4.27: Contamination on Side - effect of turbulent dispersion

Table 4.2: Wall Wetting - effect of mudrib

Wall Wetting(g)	**Driver Window**	**Total**
No Mudrib	1.15	27
Mudrib	0.06	22
Mudrib with Turbulent Dispersion modeled	0.33	24

In conclusion, the addition of turbulent dispersion affects the deposition of film downstream of the mirror. The spray-related dirt is not predicted similar to experiment but the deposition downstream of the driver window is predicted somewhat similar to the experiment. However, an ensemble averaged solution needs to be looked at in order to determine the accuracy of the turbulent dispersion model in Star-CCM+. Due to a lack of time, multiple simulations could not be performed to evaluate this.

5
Conclusion

To summarize the work, a methodology for doing Eulerian-Lagrangian simulation of rain droplets around the NEVS 9-3 model has been developed in the CFD software Star-CCM+. The methodology is used to solve for the impingement of droplets on the mirror, their transition to fluid film, the flow of the film on the mirror and its eventual separation at the edges of the mirror. The flow of the separated film in the wake of the mirror is also discussed as well as secondary breakup of droplets. It is shown how the results are highly mesh dependent. Small cells with high volume fraction for the Lagrangian parcels can create instabilities in the Lagrangian solver. Mesh refinements are needed to resolve the film flow dynamics accurately, however, the total amount of film predicted is fairly mesh independent. It has been shown how the separation of fluid film takes place from the edges of the mirror housing and how this affects the deposition of fluid film on the driver window and mirror housing. Modeling turbulent dispersion dispersion accurately was a challenge as only simple models are available in the CFD solver Star-CCM+. Finally, the results were compared to a contamination test done at NEVS.

5.1 Recommendations

To have a simulation more comparable with the climate tunnel test a simulation with similar injection point measurements as the experimental test should be performed. The injection of droplets was done assuming a constant diameter of the rain droplets. In reality a droplet size distribution must be considered. The simulation should be run for a longer physical time to have a better comparison with the contamination test. Further, the comparison between the simulations and experiments has been done only at 50 kmph. The test results are available at 30, 70 and 90 kmph as well. The simulations must be compared with the test at these velocities as well.

In this thesis, only the modeling of film around the rear view mirror housing has been considered. In reality, water flows around the A-pillar onto the driver window due to the wiper motion. Modeling this will lead to better understanding of the contamination on the driver's side window.

5.2 Future Work

In this thesis, the Eulerian-Lagrangian framework has been analyzed. However, computationally cheaper methods should be investigated in order to compare the results obtained. The reason for the differences between the experiment and simulations below the driver window needs to be analyzed in more detail. More accurate turbulent dispersion models need to be found. The thin film model which is used in this thesis can be substituted with a VOF model for higher fluid film thickness values to get more accurate results. The contact angle between the surface of the vehicle and the film determines the wettability of the surface. The contact angle has not been considered in this thesis but would play a role in determining the formation of fluid film. Using two different meshes for the Eulerian and Lagrangian phase can be investigated to get more accurate results.

Many problems in industry and academia involve multiphase flows today. This means that the modeling techniques will continue to improve not only with finite volume CFD but also other methods like Lattice Boltzmann techniques. Along with a constant increase in computational power, the multiphase flow simulations will be computationally cheaper and much more accurate.

Bibliography

[1] Bannister, M., 2000. *Drag and dirt deposition mechanisms of external rear view mirrors and techniques used for optimization.* In: SAE World Congress, Detroit, Technical Paper Series No. 2000-01-0486, pp. 97–114.

[2] Hagemeier T., Hartmann M., Thévenin D. *Practice of vehicle soiling investigations: A review.* International Journal of Multiphase Flow, 37 (2011), pp. 860–875.

[3] DrivAer Model. *Chair of Aerodynamics and Fluid mechanics, Technical University of Munich.* Accessed online 2017-06-04. URL: `https://www.aer.mw.tum.de/en/research-groups/automotive/drivaer/`

[4] CD-adapco. *User Guide*: STAR-CCM+ Version 11.06 (2016).

[5] Crowe C.T. et al, *Multiphase flows with droplets and particles.* Boca Raton, FL: CRC Press, (2012). ISBN:9781439840504, 1439840504.

[6] Maxey M., Riley J. *Equation of motion for a small rigid sphere in a non-uniform flow.* Phys. Fluids, 4 (1982). pp. 883-889.

[7] Subramaniam S. *Lagrangian-Eulerian methods for multiphase flows.* Progress In Energy and Combustion Science, (2013), pp. 215-245.

[8] Amsden A.A., O'Rourke P. J., Butler T. D., *KIVA–II: A Computer Program for Chemically Reactive Flows with Sprays*, Tech. Rep. LA–11560–MS, Los Alamos National Laboratory (May 1989)

[9] Clift R., Grace J. R., Weber M., *Bubbles, Drops and Particles*, Academic Press, (1978).

[10] Schiller L., Naumann A., *Ueber die grundlegenden Berechnungen bei der Schwerkraftaufbereitung*, VDI Zeits 77(12), (1933), pp. 318–320.

[11] Liu, A.B., Mather, D., and Reitz, R.D. 1993. *Modeling the Effects of Drop Drag and Breakup on Fuel Sprays* , SAE Paper 930072.

[12] Nourgaliev R.R, Dinh T.T, Theofanous, T.G, Joseph. D, *The lattice Boltzmann equation method: theoretical interpretation, numerics and implications*,International Journal of Multiphase Flow , 29 (2003), pp.117-169

[13] Shiyi Chen, Gary D. Doolen, *LATTICE BOLTZMANN METHOD FOR FLUID FLOWS*, Annu. Rev. Fluid Mech. 30 (1998), pp.329–64.

[14] O'Rourke, P.J., and Amsden, A.A. 1987. *The TAB Method for Numerical Calculation of Spray Droplet Breakup*, SAE Paper 872089.

[15] Chengxin Bai and Gosman A. D. 1995 *Development of Methodology for Spray Impingement Simulation*, SAE TECHNICAL PAPER SERIES 950283

[16] Mason B., Andrews J.B., *Drop-size distributions from various types of rain*, Quarterly Journal of the Royal Meteorological Society, 86 (1960) pp. 346-353.

[17] *Contamination Lab Report*, NEVS (2016)

[18] Friedrich M. A., Lan H., Wegner J. L., Drallmeier J. A. *A Separation Criterion With Experimental Validation for Shear-Driven Films in Separated Flows*, Journal of Fluid Engineering, May 2008, Vol. 130 /051301-9

[19] Baumgarten C. *Mixture Formation in Internal Combustion Engines*, Springer-Verlag Berlin Heidelberg (2006)

[20] Gosman A. D., Ioannides E.*Aspects of Computer Simulation of Liquid-Fueled Combustors*, Journal of Energy, Vol. 7, No. 6 (1983), pp. 482-490

[21] Bilanin A.J., *Scaling laws for testing airfoils under heavy rainfall*, J. Aircraft, 24 (1987), pp. 31-37.

[22] Wang, Q., Squires, K., Chen, M., McLaughlin, J., 1997. *On the role of the lift force in turbulence simulations of particle deposition.* International Journal of Multiphase Flow, 23 (1997), pp. 749–763.

[23] Persson T., *Eulerian-Lagrangian Modeling of Multicomponent Spray for Aseptic Treatment of Carton Bottles in the Food Process and Packaging Industry*, Master's Thesis in Applied Mechanics, (2013), Chalmers University of Technology
Read More: https://arc.aiaa.org/doi/10.2514/3.45407

[24] Bai C., Gosman A. D., *Modelling of Wall Films Formed by Impinging Sprays.* SAE international 960626, 1996